The Astrophysical Journal, 850:89 (30pp), 2017 November 20 https://doi.org/10.3847/1538-4357/aa8f52

Type II Supernova Spectral Diversity. I. Observations, Sample Characterization, and Spectral Line Evolution*

Claudia P. Gutiérrez[1,2,3,4], Joseph P. Anderson[3], Mario Hamuy[1,2], Nidia Morrell[5], Santiago González-Gaitan[1,6], Maximilian D. Stritzinger[7], Mark M. Phillips[5], Lluis Galbany[8], Gastón Folatelli[9], Luc Dessart[10], Carlos Contreras[5], Massimo Della Valle[11,12], Wendy L. Freedman[13], Eric Y. Hsiao[14], Kevin Krisciunas[15], Barry F. Madore[16], José Maza[2], Nicholas B. Suntzeff[15], Jose Luis Prieto[1,17], Luis González[2], Enrico Cappellaro[18], Mauricio Navarrete[5], Alessandro Pizzella[19], Maria T. Ruiz[2], R. Chris Smith[20], and Massimo Turatto[18]

[1] Millennium Institute of Astrophysics, Casilla 36-D, Santiago, Chile
[2] Departamento de Astronomía, Universidad de Chile, Casilla 36-D, Santiago, Chile
[3] European Southern Observatory, Alonso de Córdova 3107, Casilla 19, Santiago, Chile
[4] Department of Physics and Astronomy, University of Southampton, Southampton, SO17 1BJ, UK; C.P.Gutierrez-Avendano@soton.ac.uk
[5] Carnegie Observatories, Las Campanas Observatory, Casilla 601, La Serena, Chile
[6] Center for Mathematical Modelling, University of Chile, Beauchef 851, Santiago, Chile
[7] Department of Physics and Astronomy, Aarhus University, Ny Munkegade 120, DK-8000 Aarhus C, Denmark
[8] PITT PACC, Department of Physics and Astronomy, University of Pittsburgh, Pittsburgh, PA 15260, USA
[9] Facultad de Ciencias Astronómicas y Geofísicas, Universidad Nacional de La Plata, Instituto de Astrofísica de La Plata (IALP), CONICET, Paseo del Bosque SN, B1900FWA La Plata, Argentina
[10] Unidad Mixta Internacional Franco-Chilena de Astronomía (CNRS UMI 3386), Departamento de Astronomía, Universidad de Chile, Camino El Observatorio 1515, Las Condes, Santiago, Chile
[11] INAF, Osservatorio Astronomico di Capodimonte, salita Moiariello 16, I-80131 Napoli, Italy
[12] International Center for Relativistic Astrophysics, Piazzale della Repubblica 2, I-65122 Pescara, Italy
[13] Department of Astronomy and Astrophysics, University of Chicago, 5640 South Ellis Avenue, Chicago, IL 60637, USA
[14] Department of Physics, Florida State University, Tallahassee, FL 32306, USA
[15] Department of Physics and Astronomy, Texas A&M University, College Station, TX 77843, USA
[16] Observatories of the Carnegie Institution for Science, Pasadena, CA 91101, USA
[17] Núcleo de Astronomía de la Facultad de Ingeniería y Ciencias, Universidad Diego Portales, Av. Ejército 441, Santiago, Chile
[18] INAF, Osservatorio Astronomico di Padova, Vicolo dell'Osservatorio 5, 35122 Padova, Italy
[19] Dipartimento di Fisica e Astronomia—Universita di Padova, Vicolo dellOsservatorio 3, I-35122 Padova, Italy
[20] Cerro Tololo Inter-American Observatory, National Optical Astronomy Observatory, Casilla 603, La Serena, Chile
Received 2017 June 29; revised 2017 August 21; accepted 2017 September 1; published 2017 November 21

Abstract

We present 888 visual-wavelength spectra of 122 nearby type II supernovae (SNe II) obtained between 1986 and 2009, and ranging between 3 and 363 days post-explosion. In this first paper, we outline our observations and data reduction techniques, together with a characterization based on the spectral diversity of SNe II. A statistical analysis of the spectral matching technique is discussed as an alternative to nondetection constraints for estimating SN explosion epochs. The time evolution of spectral lines is presented and analyzed in terms of how this differs for SNe of different photometric, spectral, and environmental properties: velocities, pseudo-equivalent widths, decline rates, magnitudes, time durations, and environment metallicity. Our sample displays a large range in ejecta expansion velocities, from ∼9600 to ∼1500 km s^{-1} at 50 days post-explosion with a median H_α value of 7300 km s^{-1}. This is most likely explained through differing explosion energies. Significant diversity is also observed in the absolute strength of spectral lines, characterized through their pseudo-equivalent widths. This implies significant diversity in both temperature evolution (linked to progenitor radius) and progenitor metallicity between different SNe II. Around 60% of our sample shows an extra absorption component on the blue side of the H_α P-Cygni profile ("Cachito" feature) between 7 and 120 days since explosion. Studying the nature of Cachito, we conclude that these features at early times (before ∼35 days) are associated with Si II λ6355, while past the middle of the plateau phase they are related to high velocity (HV) features of hydrogen lines.

Key words: supernovae: general – surveys – techniques: photometric – techniques: spectroscopic

Supporting material: figure set, machine-readable tables

1. Introduction

Supernovae (SNe) exhibiting prevalent Balmer lines in their spectra are known as Type II SNe (SNe II henceforth, Minkowski 1941). They are produced by the explosion of massive (>8 $M_\odot$) stars, which have retained a significant part of their hydrogen envelope at the time of explosion. Red supergiant (RSG) stars have been found at the position of SN II explosion sites in pre-explosion images (e.g., Van Dyk et al. 2003; Smartt et al. 2004, 2009; Maund & Smartt 2005; Smartt 2015), suggesting that they are the direct progenitors of the vast majority of SNe II.

Initially, SNe II were classified according to the shape of the light curve: SNe with faster "linear" declining light curves were cataloged as SNe IIL, while SNe with a plateau (quasi-constant luminosity for a period of a few months) as SNe IIP (Barbon

* This paper includes data gathered with the 6.5 m *Magellan* Telescopes located at Las Campanas Observatory, Chile; and the Gemini Observatory, Cerro Pachon, Chile (Gemini Program GS-2008B-Q-56). Based on observations collected at the European Organisation for Astronomical Research in the Southern Hemisphere, Chile (ESO Programs 076.A-0156, 078.D-0048, 080.A-0516, and 082.A-0526).

et al. 1979). Years later, two spectroscopic classes and one photometric were added within the SNe II group: SNe IIn and SNe IIb, and SN 1987A-like, respectively. SNe IIn show long-lasting narrow emission lines in their spectra (Schlegel 1990), attributed to interaction with the circumstellar medium (CSM), while SNe IIb are thought to be transitional objects, between SNe II and SNe Ib (Filippenko et al. 1993). On the other hand, the 1987A-like events, following the prototype of SN 1987A (e.g., Blanco et al. 1987; Menzies et al. 1987; Hamuy et al. 1988; Phillips et al. 1988; Suntzeff et al. 1988), are spectroscopically similar to the typical SNe II; however, their light curves display a peculiar long rise to maximum (∼100 days), which is consistent with a compact progenitor. The latter three subtypes (IIn, IIb, and 87A-like) are not included in the bulk of the analysis for this paper.

Although it has been shown that SNe II[21] are a continuous single population (e.g., Anderson et al. 2014b; Sanders et al. 2015; Valenti et al. 2016), a large spectral and photometric diversity is observed. Pastorello et al. (2004) and Spiro et al. (2014) studied a sample of low luminosity SNe II. They show that these events present, in addition to low luminosities ($M_V \geqslant -15.5$ at peak), narrow spectral lines. Later, Inserra et al. (2013) analyzed a sample of moderately luminous SNe II, finding that these SNe, in contrast to the low luminosity events, are relatively bright at peak ($M_V \leqslant -16.95$).

In addition to these samples, many individual studies have been published showing spectral line identification, evolution, and parameters such as velocities and pseudo-equivalent widths (pEWs) for specific SNe. Examples of very well studied SNe include SN 1979C (e.g., Branch et al. 1981; Immler et al. 2005), SN 1980K (e.g., Buta 1982; Dwek 1983; Fesen et al. 1999), SN 1999em (e.g., Baron et al. 2000; Hamuy et al. 2001; Leonard et al. 2002b; Dessart & Hillier 2006), SN 1999gi (e.g., Leonard et al. 2002a), SN 2004et (e.g., Li et al. 2005; Sahu et al. 2006; Misra et al. 2007; Maguire et al. 2010), SN 2005cs (e.g., Pastorello et al. 2006; Dessart et al. 2008; Pastorello et al. 2009), and SN 2012aw (e.g., Bose et al. 2013; Dall'Ora et al. 2014; Jerkstrand et al. 2014). The first two SNe (1979C and 1980K) are the prototypes of fast declining SNe II (SNe IIL), together with unusually bright light curves and high ejecta velocities. On the other hand, the rest of the objects listed are generally referred to as SNe IIP, as they display relatively slowly declining light curves. For faint SNe, similar to SN 2005cs, the expansion velocity and luminosity are even lower, probably due to low energy explosions (see Pastorello et al. 2009).

In recent years, the number of studies of individual SNe II has continued to increase; however, there are still only a handful of statistical analyses of large samples (e.g., Patat et al. 1994; Arcavi et al. 2010; Anderson et al. 2014b; Faran et al. 2014b, 2014a; Gutiérrez et al. 2014; Pejcha & Prieto 2015a, 2015b; Sanders et al. 2015; Galbany et al. 2016; Müller et al. 2017; Valenti et al. 2016). Here we attempt to remedy this situation. The purpose of this paper is to present a statistical characterization of the optical spectra of SNe II, as well as an initial analysis of their spectral features. We have analyzed 888 spectra of 122 SNe II ranging between 3 and 363 days since explosion. We selected 11 features in the photospheric phase with the aim of understanding the overall evolution of visual-wavelength spectroscopy of SNe II with time.

The paper is organized as follows. In Section 2, we describe the data sample. The spectroscopic observations and data reduction techniques are presented in Section 3. In Section 4, the estimation of the explosion epoch is presented. In Section 5, we describe the sample properties, while in Section 6 we identify spectral features. The spectral measurements are presented in Section 7, while the line evolution analysis and the conclusions are in Sections 8 and 9, respectively.

In Paper II, we study the correlations between different spectral and photometric parameters, and try to understand these in terms of the diversity of the underlying physics of the explosions and their progenitors.

2. Data Sample

Our data set was obtained between 1986 and 2009 from a variety of different sources. This sample consists of 888 optical spectra of 122 SNe II,[22] of which 4 were provided by the Cerro Tololo Supernova Survey (CTSS), 7 were obtained by the Calán/Tololo survey (CT, Hamuy et al. 1993, PI: Hamuy 1989–1993), 5 by the Supernova Optical and Infrared Survey (SOIRS, PI: Hamuy, 1999–2000), 31 by the Carnegie Type II Supernova Survey (CATS, PI: Hamuy, 2002–2003), and 75 by the Carnegie Supernova Project (CSP-I, Hamuy et al. 2006, 2004–2009). These follow-up campaigns concentrated on obtaining well-sampled and high-cadence light curves and spectral sequences of nearby SNe, based mainly on two criteria: (1) that the SN was brighter than $V \sim 17$ mag at discovery and (2) that those discovered SNe were classified as being relatively young, i.e., less than one month from explosion.

The redshift distribution of our sample is shown in Figure 1. The figure shows that the majority of the sample has a redshift $\leqslant$0.03. SN 2002ig has the highest redshift in the sample with a value of 0.077, while the nearest SN (SN 2008bk) has a redshift of 0.00076. The mean redshift value of the sample is 0.0179 and the median is 0.0152. The redshift information comes from the heliocentric recession velocity of each host galaxy as published in the NASA/IPAC extragalactic Database (NED).[23] These NED values were compared with those obtained through the measurement of narrow emission lines observed within SN spectra and originating from host H II regions. In cases of discrepancy between the two sources, we give priority to our spectral estimations. Two of our objects (SN 2006Y and SN 2007ld) occur in unknown host galaxies. Their redshifts were obtained from the Asiago supernova catalog[24] and from the narrow emission lines within SN spectra originating from the underlying host galaxy, respectively. Table 1 lists the sample of SNe II selected for this work, their host galaxy information, and the campaign to which they belong.

From our SNe II sample, SNe IIn-, SNe IIb-, and SN 1987A-like events (SN 2006au and SN 2006V; Taddia et al. 2012) were excluded based on photometric information. Details of the SNe IIn sample can be found in Taddia et al. (2013), while those of the SNe IIb in Stritzinger et al. (2017)

[21] Throughout the remainder of the manuscript, we use SN II to refer to all SNe that would historically have been classified as SN IIP or SN IIL. In general, we will differentiate these events by referring to their specific light curve or spectral morphology, and we only return to this historical separation if clarification and comparison with previous works is required.

[22] In the data release, we include eight spectra of the SN 2000cb, an SN 1987A-like event, which is not analyzed in this work.

[23] http://ned.ipac.caltech.edu

[24] http://sngroup.oapd.inaf.it

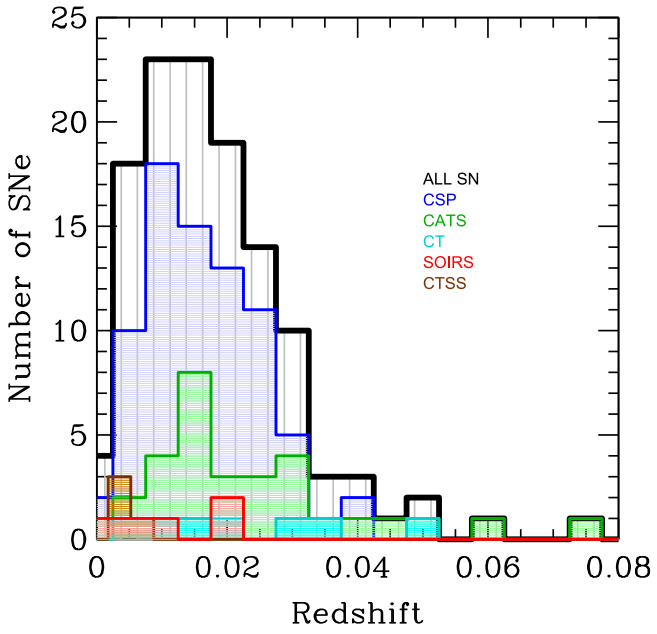

Figure 1. Distribution of heliocentric redshifts for the 122 SN II in our sample.

and Taddia et al. (2017). The photometry of our sample in the *V* band was published by Anderson et al. (2014b). More recently, Galbany et al. (2016) released the UBVRIz photometry of our sample obtained by CATS between 1986 and 2003. Around 750 spectra of ∼100 objects are published here for the first time. Now we briefly discuss each of the surveys providing SNe for our analysis.

2.1. The Cerro Tololo Supernova Survey

A total of four SNe II (SN 1986L, SN 1988A, SN 1990E, and SN 1990K) were extensively observed at CTIO by the Cerro Tololo SN program (PIs: Phillips and Suntzeff, 1986–2003). These SNe have been analyzed in previous works (e.g Schmidt et al. 1993; Turatto et al. 1993; Cappellaro et al. 1995; Hamuy 2001).

2.2. The Calán/Tololo Survey (CT)

The Calán/Tololo survey was a program of both discovery and follow-up of SNe. A total of 50 SNe were obtained between 1989 and 1993. The analysis of SNe Ia was published by Hamuy et al. (1996). Spectral and photometric details of six SNe II were presented by Hamuy (2001). In this analysis, we include these SNe II and an additional object, SN 1993K.

2.3. The Supernova Optical and Infrared Survey (SOIRS)

The Supernova Optical and Infrared Survey carried out a program to obtain optical and IR photometry and spectroscopy of nearby SNe ($z < 0.08$). In the course of 1999–2000, 20 SNe were observed, 6 of which are SNe II. Details of these SNe were published by Hamuy (2001, 2003), Hamuy et al. (2001), and Hamuy & Pinto (2002).

2.4. The Carnegie Type II Supernova Survey (CATS)

Between 2002 and 2003 the Carnegie Type II Supernova Survey observed 34 SNe II. While optical spectroscopy and photometry of these SNe II have been previously used to derive distances (Olivares 2008; Jones et al. 2009), the spectral observations have not been officially released until now.

2.5. The Carnegie Supernova Project I (CSP-I)

The Carnegie Supernova Project I (CSP-I) was a five-year follow-up program to obtain high quality optical and near-infrared light curves and optical spectroscopy. The data obtained by the CSP-I between 2004 and 2009 consist of ∼250 SNe of all types, of which 75 correspond to SNe II. The first SN Ia photometry data were published in Contreras et al. (2010), while their analysis was done by Folatelli et al. (2010). A second data release was provided by Stritzinger et al. (2011). A spectroscopy analysis of SNe Ia was published by Folatelli et al. (2013). Recently, Stritzinger et al. (2017) and Taddia et al. (2017) published the photometry data release of stripped-envelope supernovae. The CSP-I spectral data for SNe II are published here for the first time, while the complete optical and near-IR photometry will be published by C. Contreras et al. (2017, in preparation).

3. Observations and Data Reduction

In this section, we summarize our observations and the data reduction techniques. However, a detailed description of the CT methodology is presented in Hamuy et al. (1993), for the case of SOIRS the CT methodology is described in Hamuy et al. (2001), and for CSP-I it can be found in Hamuy et al. (2006) and Folatelli et al. (2013).

3.1. Observations

The data presented here were obtained with a large variety of instruments and telescopes, as shown in Table 6. The majority of the spectra were taken in long-slit spectroscopic mode with the slit placed along the parallactic angle. However, when the SN was located close to the host, it was necessary to pick a different and more convenient angle to avoid contamination from the host. The majority of our spectra cover the range of ∼3800 to ∼9500 Å. The observations were performed with the Cassegrain spectrographs at 1.5 m and 4.0 m telescopes at Cerro Tololo, with the Wide Field CCD Camera (WFCCD) at the 2.5 m du Pont Telescope, the Low Dispersion Survey Spectrograph (LDSS2; Allington-Smith et al. 1994) on the *Magellan* Clay 6.5 m telescope and the Inamori *Magellan* Areal Camera and Spectrograph (IMACS; Dressler et al. 2011) on the *Magellan* Baade 6.5 m telescope at Las Campanas Observatory. At La Silla, the observations were carried out with the ESO Multi-Mode Instrument (EMMI; Dekker et al. 1986) in medium resolution spectroscopy mode (at the NTT) and the ESO Faint Object Spectrograph and Camera (EFOSC; Buzzoni et al. 1984) at the NTT and 3.6 m telescopes. We also have three spectra for SN 2006ee obtained with the Boller & Chivens CCD spectrograph at the Hiltner 2.4 m Telescope of the MDM Observatory. Table 6 displays a complete journal of the 888 spectral observations, listing for each spectrum the UT and Julian dates, phases, wavelength range, FWHM resolution, exposure time, airmass, and the telescope and instrument used.

The distribution of the number of spectra per object for our sample is shown in Figure 2. Seven SNe (SN 1993A, SN 2005dt, SN 2005dx, SN 2005es, SN 2005gz, SN 2005me, and SN 2008H) only have one spectrum, while 90% of the sample have between 2 and 12 spectra. SN 1986L is the object

Table 1
SN II Sample

SN	Host Galaxy	Recession Velocity (km s^{-1})	Hubble Type	$E(B-V)_{MW}$ (mag)	Discovery Date	Discovery Reference	Explosion Epoch	N of Spectra	Campaign
1986L	NGC 1559	1305	SBcd	0.026	46711.1	IAUC 4260	46708.0[a](3)	31	CTSS
1988A	NGC 4579	1517	SABb	0.036	47179.0	IAUC 4533	47177.2[a](2)	5	CTSS
1990E	NGC 1035	1241	SAc	0.022	47937.7	IAUC 4965	47935.1[a](3)	5	CTSS
1990K	NGC 0150	1584	SBbc	0.013	48037.3	IAUC 5022	48001.5[a](6)	9	CTSS
1991al	2MASX J19422191-5506275	4575[b]	?	0.054	48453.7	IAUC 5310	48442.5[c](8)[d]	8	CT
1992af	ESO 340-G038	5541	S	0.046	48802.8	IAUC 5554	48798.8[c](8)[d]	5	CT
1992am	MCG -01-04-039	14397[b]	S	0.046	48829.8	IAUC 5570	48813.9[c](6)[d]	2	CT
1992ba	NGC 2082	1185	SABc	0.051	48896.2	IAUC 5625	48884.9[c](7)	10	CT
1993A	2MASX J07391822-6203095	8790[b]	?	0.153	49004.6	IAUC 5693	48995.5[a](9)	2	CT
1993K	NGC 2223	2724	SBbc	0.056	49075.5	IAUC 5733	49065.5[a](9)	17	CT
1993S	2MASX J22522390-4018432	9903	S	0.014	49133.7	IAUC 5812	49130.8[c](5)	4	CT
1999br	NGC 4900	960	SBc	0.021	51281.0	IAUC 7141	51276.7[a](4)	8	SOIRS
1999ca	NGC 3120	2793	Sc	0.096	51296.0	IAUC 7158	51277.5[c](7)[d]	4	SOIRS
1999cr	ESO 576-G034	6069[b]	S/Irr	0.086	51249.7	IAUC 7210	51246.5[c](4)[d]	5	SOIRS
1999eg	IC 1861	6708	SA0	0.104	51455.5	IAUC 7275	51449.5[c](6)[d]	2	SOIRS
1999em	NGC 1637	717	SABc	0.036	51481.0	IAUC 7294	51476.5[a](5)	12	SOIRS
2002ew	NEAT J205430.50-000822.0	8975	?	0.091	52510.8	IAUC 7964	52500.6[a](10)	7	CATS
2002fa	NEAT J205221.51 + 020841.9	17988	?	0.088	52510.8	IAUC 7967	52502.5[c](8)[d]	6	CATS
2002gd	NGC 7537	2676	SAbc	0.059	52552.7	IAUC 7986	52551.5[c](4)[d]	12	CATS
2002gw	NGC 922	3084	SBcd	0.017	52560.7	IAUC 7995	52553.5[c](8)[d]	11	CATS
2002hj	NPM1G +04.0097	7080	?	0.102	52568.0	IAUC 8006	52562.5[a](7)	7	CATS
2002hx	PGC 023727	9293	SBb	0.048	52589.7	IAUC 8015	52582.5[a](9)	9	CATS
2002ig	SDSS J013637.22 + 005524.9	23100[e]	?	0.034	52576.7	IAUC 8020	52570.5[c](5)[d]	5	CATS
210	MCG +00-03-054	15420	?	0.033	?[f]	?	52486.5[c](6)[d]	6	CATS
2003B	NGC 1097	1272	SBb	0.024	52645.0	IAUC 8042	52613.5[c](11)[d]	9	CATS
2003E	MCG -4-12-004	4470[b]	Sbc	0.043	52645.0	IAUC 8044	52629.5[c](8)[d]	8	CATS
2003T	UGC 4864	8373	SAab	0.028	52665.0	IAUC 8058	52654.5[a](10)	6	CATS
2003bl	NGC 5374	4377[b]	SBbc	0.024	52701.0	IAUC 8086	52696.5[c](4)[d]	8	CATS
2003bn	2MASX J10023529-2110531	3828	?	0.057	52698.0	IAUC 8088	52694.5[a](3)	12	CATS
2003ci	UGC 6212	9111	Sb	0.053	52720.0	IAUC 8097	52711.5[a](8)	7	CATS
2003cn	IC 849	5433[b]	SABcd	0.019	52728.0	IAUC 8101	52717.5[c](4)[d]	5	CATS
2003cx	NEAT J135706.53-170220.0	11100	?	0.083	52730.0	IAUC 8105	52725.5[c](5)[d]	6	CATS
2003dq	MAPS-NGP O4320786358	13800	?	0.016	52739.7	IAUC 8117	52731.5[a](8)	3	CATS
2003ef	NGC 4708	4440[b]	SAab	0.041	52770.7	IAUC 8131	52757.5[c](9)[d]	6	CATS
2003eg	NGC 4727	4388[b]	SABbc	0.046	52776.7	IAUC 8134	52764.5[c](5)[d]	5	CATS
2003ej	UGC 7820	5094	SABcd	0.017	52779.7	IAUC 8134	52775.5[a](5)	3	CATS
2003fb	UGC 11522	5262[b]	Sbc	0.162	52796.0	IAUC 8143	52772.5[c](10)[d]	4	CATS
2003gd	M74	657	SAc	0.062	52803.2	IAUC 8150	52755.5[c](9)[d]	3	CATS
2003hd	MCG -04-05-010	11850	Sb	0.011	52861.0	IAUC 8179	52855.9[c](5)[d]	9	CATS
2003hg	NGC 7771	4281	SBa	0.065	52870.0	IAUC 8184	52865.5[a](5)	5	CATS
2003hk	NGC 1085	6795	SAbc	0.033	52871.6	CBET 41	52866.8[c](4)[d]	4	CATS
2003hl	NGC 772	2475	SAb	0.064	52872.0	IAUC 8184	52868.5[a](5)	6	CATS
2003hn	NGC 1448	1170	SAcd	0.013	52877.2	IAUC 8186	52866.5[a](10)	9	CATS
2003ho	ESO 235-G58	4314	SBcd	0.034	52851.9	IAUC 8186	52848.5[c](7)[d]	5	CATS
2003ib	MCG -04-48-15	7446	Sb	0.043	52898.7	IAUC 8201	52891.5[a](8)	5	CATS
2003ip	UGC 327	5403	Sbc	0.058	52913.7	IAUC 8214	52896.5[c](4)	4	CATS
2003iq	NGC 772	2475	SAb	0.064	52921.5	CBET 48	52919.5[a](2)	5	CATS
2004dy	IC 5090	9352	Sa	0.045	53242.5	IAUC 8395	53240.5[a](2)	3	CSP
2004ej	NGC 3095	2723	SBc	0.061	53258.5	CBET 78	53223.9[c](9)[d]	9	CSP
2004er	MCG -01-7-24	4411	SAc	0.023	53274.0	CBET 93	53271.8[a](2)	10	CSP
2004fb	ESO 340-G7	6100	S	0.056	53286.2	IAUC 8420	53258.6[c](7)[d]	4	CSP
2004fc	NGC 701	1831	SBc	0.023	53295.2	IAUC 8422	53293.5[a](1)	10	CSP
2004fx	MCG -02-14-3	2673	SBc	0.090	53307.0	IAUC 8431	53303.5[a](4)	10	CSP
2005J	NGC 4012	4183	Sb	0.025	53387.0	IAUC 8467	53379.8[c](7)[d]	11	CSP
2005K	NGC 2923	8204	?	0.035	53386.0	IAUC 8468	53369.8[c](8)	2	CSP
2005Z	NGC 3363	5766	S	0.025	53402.0	IAUC 8476	53396.7[a](6)	9	CSP
2005af	NGC 4945	563	SBcd	0.156	53409.7	IAUC 8482	53320.8[c](17)[d]	9	CSP
2005an	ESO 506-G11	3206	S0	0.083	53432.7	CBET 113	53431.8[c](6)[d]	7	CSP
2005dk	IC 4882	4708	SBb	0.043	53604.0	IAUC 8586	53601.5[c](6)[d]	7	CSP

Table 1
(Continued)

SN	Host Galaxy	Recession Velocity (km s^{-1})	Hubble Type	$E(B-V)_{\rm MW}$ (mag)	Discovery Date	Discovery Reference	Explosion Epoch	N of Spectra	Campaign
2005dn	NGC 6861	2829	SA0	0.048	53609.5	IAUC 8589	53602.6[c](6)[d]	8	CSP
2005dt	MCG -03-59-6	7695	SBb	0.025	53614.7	CBET 213	53605.6[a](9)	1	CSP
2005dw	MCG -05-52-49	5269	Sab	0.020	53612.7	CBET 219	53603.6[a](9)	3	CSP
2005dx	MCG -03-11-9	8012	S	0.021	53623.0	CBET 220	53611.8[c](7)[d]	1	CSP
2005dz	UGC 12717	5696	Scd	0.072	53623.7	CBET 222	53619.5[a](4)	7	CSP
2005es	MCG +01-59-79	11287	S	0.076	53643.7	IAUC 8608	53638.7[a](5)	1	CSP
2005gz	MCG -01-53-022	8518	SBbc	0.06	53654.7	IAUC 8616	53650.2[a](5)	1	CSP
2005lw	IC 672	7710	?	0.043	53719.0	CBET 318	53716.8[c](10)	14	CSP
2005me	ESO 244-31	6726	SAc	0.022	53728.2	CBET 333	53717.9[c](10)[d]	1	CSP
2006Y	anon	10074[e]	?	0.115	53770.0	IAUC 8668	53766.5[a](4)	13	CSP
2006ai	ESO 005-G009	4571[b]	SBcd	0.113	53784.0	CBET 406	53781.6[c](5)	12	CSP
2006bc	NGC 2397	1363	SABb	0.181	53819.1	CBET 446	53815.5[a](4)	3	CSP
2006be	IC 4582	2145	S	0.026	53819.0	CBET 449	53802.8[c](9)[d]	4	CSP
2006bl	MCG +02-40-9	9708	?	0.045	53829.5	CBET 597	53822.7[c](10)[d]	3	CSP
2006ee	NGC 774	4620	S0	0.054	53966.0	cbet 597	53961.9[a](4)	13	CSP
2006it	NGC 6956	4650	SBb	0.087	54009.5	CBET 660	54006.5[a](3)	6	CSP
2006iw	2MASX J23211915 + 0015329	9226	?	0.044	54011.5	CBET 663	54010.7[a](1)	5	CSP
2006ms	NGC 6935	4543	SAa	0.031	54046.2	CBET 725	54028.5[c](6)[**]	4	CSP
2006qr	MCG -02-22-023	4350	SABbc	0.040	54070.0	CBET 766	54062.8[a](7)	8	CSP
2007P	ESO 566-G36	12224	Sa	0.036	54124.0	CBET 819	54118.7[a](5)	6	CSP
2007U	ESO 552-65	7791	S	0.046	54136.5	CBET 835	54133.6[c](6)[d]	7	CSP
2007W	NGC 5105	2902	SBc	0.045	54146.5	CBET 844	54130.8[c](7)[d]	7	CSP
2007X	ESO 385-G32	2837	SABc	0.060	54146.5	CBET 844	54143.5[c](5)	12	CSP
2007Z	PGC 016993	5277	Sbc	0.525	54148.7	CBET 847	54135.6[c](5)	2	CSP
2007aa	NGC 4030	1465	SAbc	0.023	54149.7	CBET 848	54126.7[c](8)[d]	11	CSP
2007ab	MCG -01-43-2	7056	SBbc	0.235	54150.7	CBET 851	54123.9[c](10)	5	CSP
2007av	NGC 3279	1394	Scd	0.032	54180.2	CBET 901	54173.8[c](5)[d]	4	CSP
2007bf	UGC 09121	5327	Sbc	0.018	54285.0	CBET 919	54191.5[a](7)	4	CSP
2007hm	SDSS J205755.65-072324.9	7540	?	0.059	54343.7	CBET 1050	54336.6[c](6)[d]	7	CSP
2007il	IC 1704	6454	S	0.042	54354.0	CBET 1062	54349.8[a](4)	12	CSP
2007it	NGC 5530	1193	SAc	0.103	54357.5	CBET 1065	54348.5[a](1)	11	CSP
2007ld	anon	7499[b]	?	0.081	54379.5	CBET 1098	54376.5[c](8)[d]	7	CSP
2007oc	NGC 7418	1450	SABcd	0.014	54396.5	CBET 1114	54388.5[a](3)	17	CSP
2007od	UGC 12846	1734	Sm	0.032	54407.2	CBET 1116	54400.6[c](5)[d]	14	CSP
2007sq	MCG -03-23-5	4579	SAbc	0.183	54443.0	CBET 1170	54422.8[c](6)[d]	7	CSP
2008F	MCG -01-8-15	5506	SBa	0.044	54477.5	CBET 1207	54469.6[c](6)[d]	2	CSP
2008H	ESO 499- G 005	4287	SAc	0.057	54481.0	CBET 1210	54432.8[c](8)	1	CSP
2008K	ESO 504-G5	7997	Sb	0.035	54481.0	CBET 1211	54475.5[c](6)[d]	12	CSP
2008M	ESO 121-26	2267	SBc	0.040	54480.7	CBET 1214	54471.7[a](9)	12	CSP
2008W	MCG -03-22-7	5757	Sc	0.086	54502.7	CBET 1238	54483.8[c](8)[d]	10	CSP
2008ag	IC 4729	4439	SABbc	0.074	54499.5	CBET 1252	54477.9[c](8)[d]	18	CSP
2008aw	NGC 4939	3110	SAbc	0.036	54528.0	CBET 1279	54517.8[a](10)	12	CSP
2008bh	NGC 2642	4345	SBbc	0.020	54549.0	CBET 1311	54543.5[a](5)	6	CSP
2008bk	NGC 7793	227	SAd	0.017	54550.7	CBET 1315	54540.9[c](8)[d]	26	CSP
2008bm	CGCG 071-101	9563	Sc	0.023	54554.7	CBET 1320	54522.8[c](6)	4	CSP
2008bp	NGC 3095	2723	SBc	0.061	54558.7	CBET 1326	54551.7[a](6)	5	CSP
2008br	IC 2522	3019	SAcd	0.083	54564.2	CBET 1332	54555.7[a](9)	4	CSP
2008bu	ESO 586-G2	6630	S	0.376	54574.0	CBET 1341	54566.8[c](7)	5	CSP
2008ga	LCSB L0250N	4639	?	0.582	54734.0	CBET 1526	54711.5[c](7)	3	CSP
2008gi	CGCG 415-004	7328	Sc	0.060	54752.0	CBET 1539	54742.7[a](9)	6	CSP
2008gr	IC 1579	6831	SBbc	0.012	54768.7	CBET 1557	54769.6[c](6)[d]	5	CSP
2008hg	IC 1720	5684	Sbc	0.016	54785.5	CBET 1571	54779.8[a](5)	6	CSP
2008ho	NGC 922	3082	SBcd	0.017	54796.5	CBET 1587	54792.7[a](5)	3	CSP
2008if	MCG -01-24-10	3440	Sb	0.029	54812.7	CBET 1619	54807.8[a](5)	20	CSP
2008il	ESO 355-G4	6276	SBb	0.015	54827.7	CBET 1634	54825.6[a](3)	3	CSP
2008in	NGC 4303	1566	SABbc	0.020	54827.2	CBET 1636	54825.4[a](2)[d]	13	CSP
2009N	NGC 4487	1034	SABcd	0.019	54856.3	CBET 1670	54846.8[c](5)	13	CSP
2009W	SDSS J162346.79 + 114423	5100	?	0.065	54865.0	CBET 1683	54816.9[c](9)	1	CSP
2009aj	ESO 221- G 018	2883	Sa	0.130	54887.0	CBET 1704	54880.5[a](7)	12	CSP

Table 1
(Continued)

SN	Host Galaxy	Recession Velocity (km s^{-1})	Hubble Type	$E(B-V)_{MW}$ (mag)	Discovery Date	Discovery Reference	Explosion Epoch	N of Spectra	Campaign
2009ao	NGC 2939	3339	Sbc	0.034	54895.0	CBET 1711	54890.7[a](4)	7	CSP
2009au	ESO 443-21	2819	Scd	0.081	54902.0	CBET 1719	54897.5[a](4)	10	CSP
2009bu	NGC 7408	3494	SBc	0.022	54916.2	CBET 1740	54901.9[c](8)[d]	6	CSP
2009bz	UGC 9814	3231	Sdm	0.035	54920.0	CBET 1748	54915.8[a](4)	5	CSP

Notes. *Observing campaigns:* CTSS = Cerro Tololo Supernova Survey; CT = Calán/Tololo Supernova Program; SOIRS = Supernova Optical and Infrared Survey; CATS = Carnegie Type II Supernova Survey; CSP = Carnegie Supernova Project.
In the first column, the SN name, followed by its host galaxy are listed. In column 3, we list the host galaxy heliocentric recession velocity. These are taken from the NASA Extragalactic Database (NED: http://ned.ipac.caltech.edu/) unless indicated by a superscript (sources in table notes). In columns 4 and 5, we list the host galaxy morphological Hubble types (from NED) and the reddening due to dust in our Galaxy (Schlafly & Finkbeiner 2011) taken from NED. In columns 6, 7, and 8, we list the discovery date, their reference, and the explosion epochs. The number of spectra and the the observing campaign from which each SN was taken are given in columns 9 and 10, and acronyms are listed in the table notes.
[a] Explosion epoch estimation from SN nondetection.
[b] Measured using our own spectra.
[c] Explosion epoch estimation through spectral matching.
[d] Cases where explosion epochs have changed between Anderson et al. (2014b) and the current work.
[e] Taken from the Asiago supernova catalog: http://graspa.oapd.inaf.it/ (Barbon et al. 1999).
[f] The CATS survey performed the follow-up of SN 210, which was discovered by the SN Factory Wood-Vasey et al. (2004) and was never reported to the International Astronomical Union (IAU) to provide an official designation.

(This table is available in machine-readable form.)

with the most spectra (31), followed by SN 2008bk with 26. On average, we have 7 spectra per SN and a median of 6. There are 87 SNe II for which we have five or more spectra, 32 that have 10 or more, and 6 objects with over 15 spectra (SN 1986L, SN 1993K, SN 2007oc, SN 2008ag, SN 2008bk, and SN 2008if). In the current work, 4% of our obtained spectra are not used for analysis. 3% correspond to spectra with low S/N that does not allow for useful extraction of our defined parameters, while 1% are related with peculiarities in the spectra (see Section 5 for more details). Despite this, these spectra are still included in the data release and are noted in Table 6.

3.2. Data Reduction

Spectral reduction was achieved in the same manner for all data, using IRAF and employing standard routines, including bias subtraction, flat-fielding correction, one-dimensional (1D) spectral extraction and sky subtraction, wavelength correction, and flux calibration. Telluric corrections have only been applied to data obtained after 2004 October.

In Appendix A (spectral series), we show plots with the spectral series for all SNe of our sample.

4. Explosion Epoch Estimations

Before discussing the properties of our sample, in this section, we outline our methods for estimating explosion epochs. The nondetection of SNe on prediscovery images with high cadence is the most accurate method for determining the explosion epoch for any given SN. Explosion epochs based on nondetections are set to the midpoint between SN discovery and nondetection. The representative uncertainty on this epoch is then $(MJD_{disc}–MJD_{non\text{-}det})/2$. However, within our sample (and for many other current SN search campaigns) many SNe do not have such accurate constraints from this method due to the low cadence of the observations.

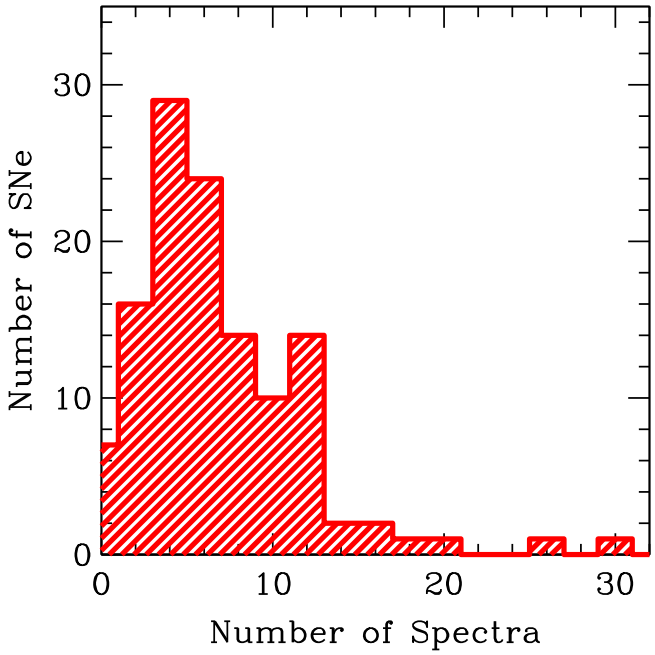

Figure 2. Histogram of the number of spectra per SN. The distribution peaks at four spectra.

Over the last decade, several tools have been published, enabling explosion epoch estimations through matching of observed SN spectra to libraries of spectral templates. Programs such as the Supernova Identification (SNID) code (Blondin & Tonry 2007), the GEneric cLAssification TOol (Gelato; Harutyunyan et al. 2008), and superfit (Howell et al. 2005) allow the user to estimate the type of supernova and its epoch by providing an observed spectrum. All perform classifications by comparison using different methods. In our analysis, we used only the first two methods: SNID and Gelato.

We find that Gelato gives a large percentage of their quality of fit to the H_α P-Cygni profile. However, based on our analysis (see Section 8), the most significant changes with time are observed in the blue part of the spectra (i.e., between 4000 and 6000 Å). Moreover, according to Gutiérrez et al. (2014), the H_α P-Cygni profile shows a wide diversity and there is no clear, consistent evolution with time. In addition, SNID provides the possibility of adding additional templates to improve the accuracy of explosion epoch determinations. We take advantage of this attribute in the following sections by adding new spectral templates, which aid in obtaining more accurate explosion epochs for our sample.

While for many SNe this spectral matching is required to obtain a reliable explosion epoch, a significant fraction of our sample does have an explosion epoch, constraining SN nondetections before discovery. In cases where the nondetection is <20 days before discovery, we use that information to estimate our final values. In cases where this difference is larger than 20 days, we use the spectral matching technique. As a test of our methodology, for nondetection SNe, we also estimate explosion epochs using spectral matching to check the latter's validity (see below for more details).

4.1. SNID Implementation

To constrain the explosion epoch for our sample, we compare the first spectrum of each SN II with a library of spectral templates provided by SNID and then, we choose the best match. For each SN, we examined multiple matches, putting emphasis on the fit of the blue part of the spectrum between 4000 and 6000 Å. This region contains many spectral lines that display a somewhat consistent evolution with time, unlike the dominant H_α profile at redder wavelengths. Explosion epoch errors from this spectral matching are obtained by taking the standard deviation of several good matches of the observed spectrum of our selected object with those from the SNID library. H_α is the dominant feature in SN II spectra; however, its evolution and morphology varies greatly between SNe in a manner that does not aid in the spectral matching technique. We therefore ignore this wavelength region.

The red part of the spectrum can be ignored during spectral matching in a variety of ways: (1) using the SNID options; or (2) checking only the match in the blue part. For the former, SNID gives to the user the alternative to modify some parameters. In our case, we can constrain the wavelength range using *wmin* and *wmax*. Hence, the structure used is *"snid wmin = 3500 wmax = 6000 spec.dat"*. For the latter, we just need to ignore visually the red part of the spectra and explore the matches obtained by SNID until we find a good fit in the blue part.[25]

From the SNID library, we use those template SNe that have well constrained explosion epochs, meaning SNe II with explosion epoch errors of less than five days (see Table 2). Specifically, we used SN 1999em (Leonard et al. 2002b), SN 1999gi (Leonard et al. 2002a), SN 2004et (Li et al. 2005), SN 2005cs (Pastorello et al. 2006), and SN 2006bp (Dessart et al. 2008). In the database of SNID, there are a total of 166 spectra. However, these templates do not provide a good coverage of the overall diversity of SNe II within our sample/the literature. Most of the SNe in the library are relatively "normal," with only one subluminous event (SN 2005cs). This means that any non-normal event within our sample will probably have poor constraints on its explosion epoch using these templates. For this reason, we decided to use some of our own well-observed SNe II to complement the SNID database.

[25] Note that the results obtained from the spectral matching are not altered if you use either all of the visible wavelength spectrum or just the region between 4000 and 6000.

Table 2
Reference SNe II

SN	Explosion Date	V-maximum Date	Days from Explosion to V-maximum	References
1999em	2451475.6 (5)	2451485.5	5	Leonard et al. (2002b)
1999gi	2451518.3 (3)	2451530.0	12	Leonard et al. (2002a)
2004et	2453270.5 (3)	2453286.6	16	Li et al. (2005), Sahu et al. (2006)
2005cs	2453547.6 (1)	2453553.6	6	Pastorello et al. (2006)
2006bp	2453833.4 (1)	2453842.0	9	Dessart et al. (2008)
1988A	2447177.2 (2)	···	···	This work
1990E	2447935.1 (3)	···	···	This work
1999br	2451276.7 (4)	···	···	This work
2003bn	2452694.5 (3)	···	···	This work
2003iq	2452919.5 (2)	···	···	This work
2004er	2453271.8 (2)	···	···	This work
2004fc	2453293.5 (1)	···	···	This work
2004fx	2453303.5 (4)	···	···	This work
2005dz	2453619.5 (4)	···	···	This work
2006bc	2453815.5 (4)	···	···	This work
2006ee	2453961.9 (4)	···	···	This work
2006it	2454006.5 (3)	···	···	This work
2006iw	2454010.7 (1)	···	···	This work
2006Y	2453766.5 (4)	···	···	This work
2007il	2454349.8 (4)	···	···	This work
2007it	2454348.5 (1)	···	···	This work
2007oc	2454388.5 (3)	···	···	This work
2008il	2454825.6 (3)	···	···	This work
2008in	2454825.4 (2)	···	···	This work
2009ao	2454890.7 (4)	···	···	This work
2009au	2454897.5 (4)	···	···	This work
2009bz	2454915.8 (4)	···	···	This work

Note. Columns: (1) SN name; (2) Julian date of the explosion epoch; (3) Julian date of the *V*-band maximum; (4) days from Explosion to *V*-band maximum; (5) references.
The first five SNe are included in SNID and are used as templates in this work. Their respective references are presented in column 4. The rest of the SNe showed after the line are taken from this work as new SNID templates.

4.2. New SNID Templates

We created a new set of spectral templates using our own SNe II nondetection limits. SNe II are included as new SNID templates if they have errors on explosion epochs (through nondetection constraints) of less than five days. Given this criterion, we included 22 SNe, which show significant spectral and photometric diversity. In this manner, the new SNID templates were constructed using ∼150 spectra and prepared using the *logwave* program included in the SNID packages.

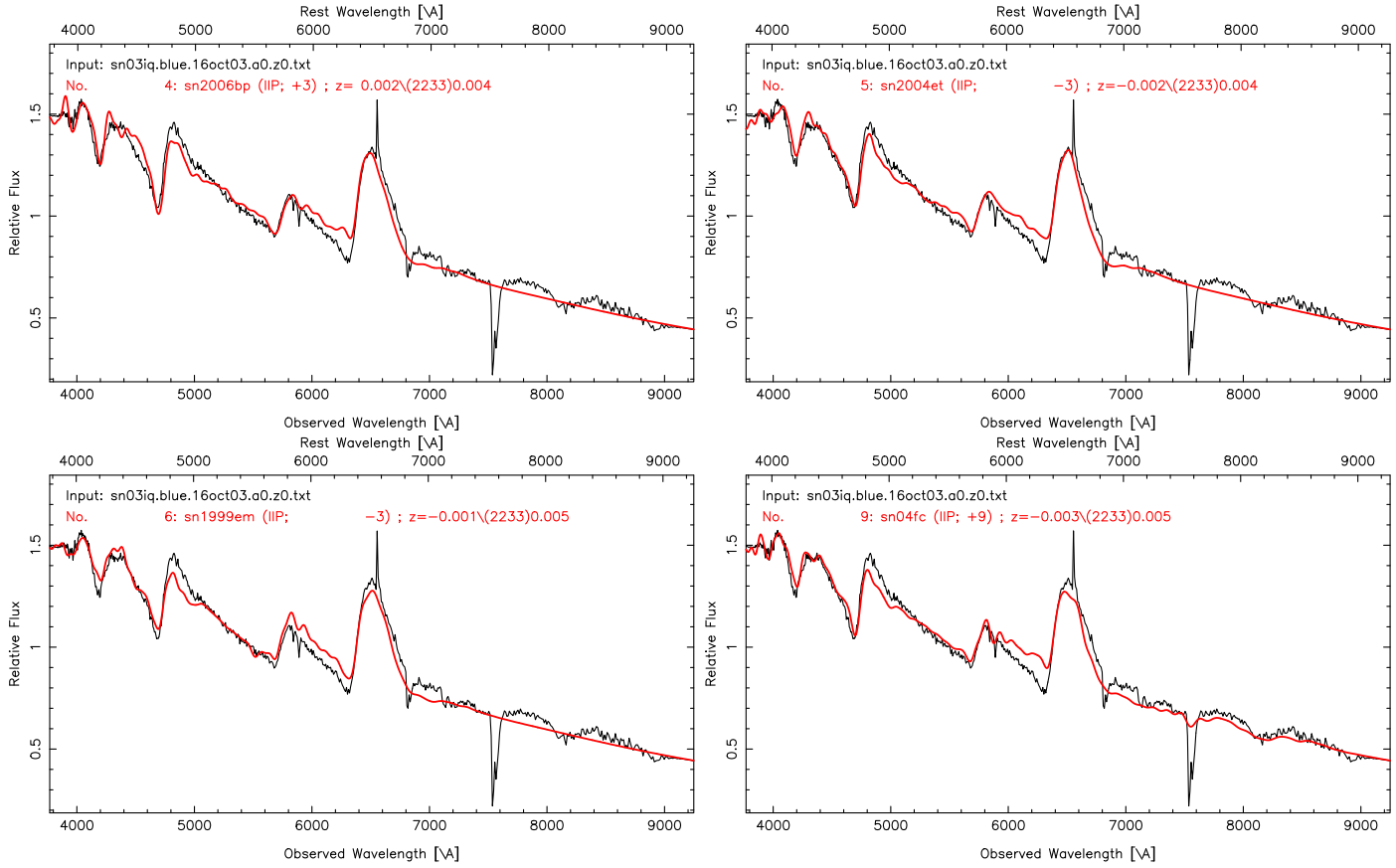

Figure 3. Best spectral matching of SNe 2003iq using SNID. The plots show SN 2003iq compared with SN 2006bp, SN 2004et, SN 1999em, and SN 2004fc at 3, −3 and −3 and 9 days. As the first three SNe are included in the SNID database, they are in respect of the maximum, hence we have to add to them the days between the explosion and the *V*-band maximum (see Table 2) to obtain the explosion epoch. On the other hand, SN 2004fc (included in this work) is in respect of the explosion. Therefore, SN 2003iq has a good match with these SNe at 12, 13, 7, and 9 days from explosion, respectively. Taking the average, this means that this spectrum is at 10 ± 7 days from explosion.

Adding our own template SNe to the SNID database, we can now use a total of 27 template SNe II to estimate the explosion epoch. Table 2 shows the explosion epoch and the maximum dates in *V*-band for the reference SNe, as well as the explosion epoch for our new templates. We note an important difference between our templates and previous ones in SNID: for the newer templates, epochs are labeled with respect to the explosion epoch, while for the older templates epochs are labeled with respect to maximum light (meaning that one then has to add the "rise time" to obtain the actual explosion date, see Table 2).

4.3. Explosion Epochs for the Current Sample

With the inclusion of these 22 SNe to SNID, we estimated the explosion epoch for our full sample. An example of the best match is shown in Figure 3. We can see that the first spectrum of SN 2003iq (October 16th) is best matched with SN 2006bp, SN 2004et, SN 1999em, and SN 2004fc 12, 13, 7, and 9 days from explosion, respectively. Taking the average, we conclude that the spectrum was obtained at 10 ± 7 days since the explosion. Table 1 shows the explosion epoch for each SN as well as the method employed to derive it, while Table 7 shows all the details of spectral matching and nondetection techniques. Appendix B (SNID matches) shows the plots with the best matches for each SN in our sample.

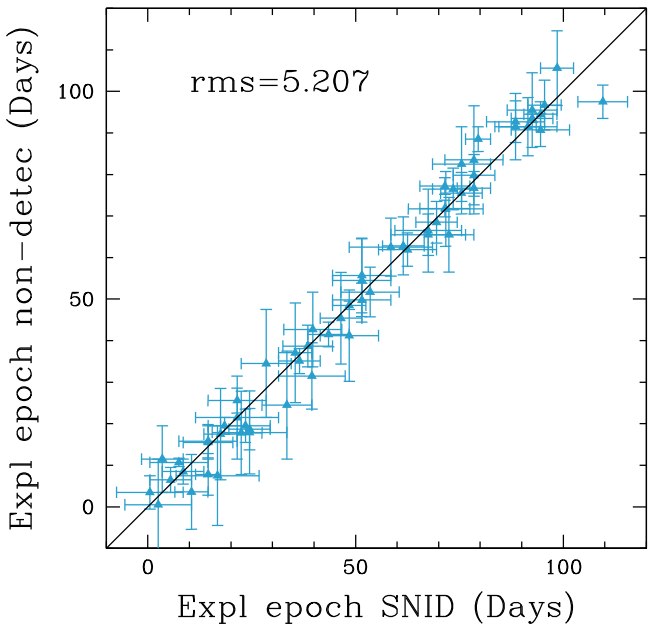

Figure 4. Comparison between spectral matching and nondetection methods.

To check the validity of spectral matching, we compare the explosion epoch estimated with this technique and those with nondetections. These two estimations are displayed in Table 7.

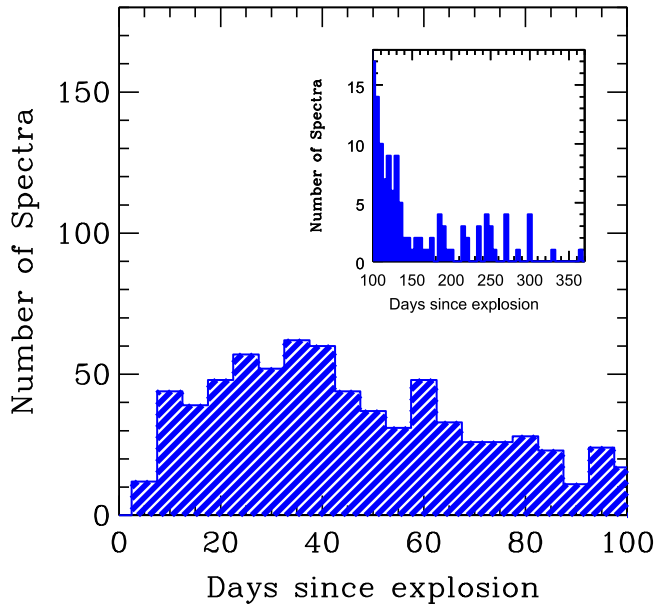

Figure 5. Distribution of the number of spectra as a function of epoch from explosion. The inset on the right shows the same distribution between 100 and 370 days.

From the second to the seventh column, the spectral matching details are shown (spectrum date, best match found, days from maximum—from the SNID templates—days from explosion, average, and explosion date), while from eighth to tenth, those obtained from the nondetection (nondetection date, discovery date, and explosion date). The differences between both methods are presented in the last column. Such an analysis was previously performed by Anderson et al. (2014b), where good agreement was found. With the use of our new templates, we are able to improve the agreement between different explosion epoch constraining methods, thus justifying their inclusion. Figure 4 shows a comparison between both methods, where the mean absolute error between them diminishes from 4.2 (Anderson et al. 2014b) to 3.9 days. Also the mean offset decreases from 1.5 days in Anderson et al. (2014b) to 0.5 days in this work. Cases where explosion epochs have changed between Anderson et al. (2014b) and the current work are noted in Table 1. Nevertheless, although this method works well as a substitute for nondetections, exact constraints for any particular object are affected by any peculiarities inherent to the observed (or indeed template) SN. For example, differences in the color (and therefore temperature) evolution of events can mimic differences in time evolution, while progenitor metallicity differences can delay/hasten the onset of line formation. Further improvements of this technique can only be obtained by the inclusion of additional, well-observed SNe II in the future.

5. Sample Properties

As mentioned in Section 2, we have 888 optical spectra of 122 SNe II; however, due to low signal-to-noise (S/N), we remove 26 spectra of 12 SNe for our analysis. We also remove nine spectra of SN 2005lw because they contain peculiarities that we expect are not intrinsic to the SN (most probably defects resulting from the observing procedure or data reduction). In total, we remove 35 spectra (∼4%). Figure 5 shows the epoch distribution of our spectra since explosion to

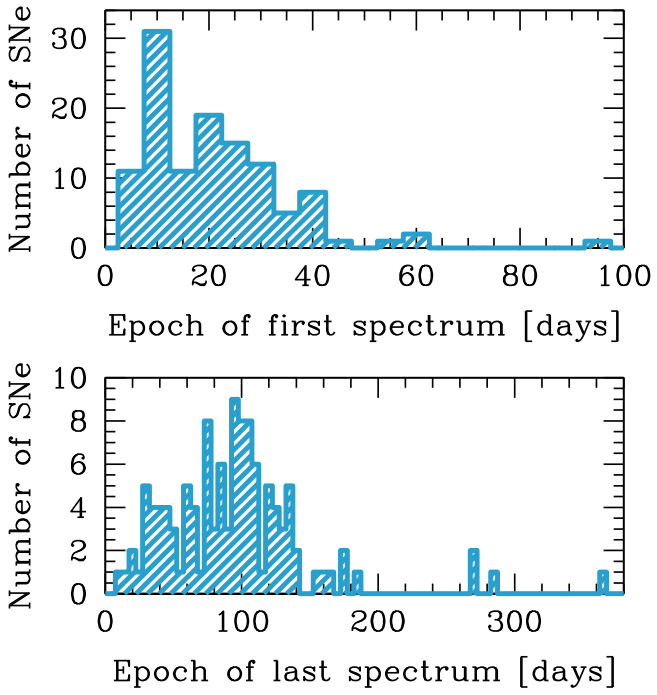

Figure 6. Top: epoch from explosion of first spectrum. Bottom: epoch from explosion of last spectrum.

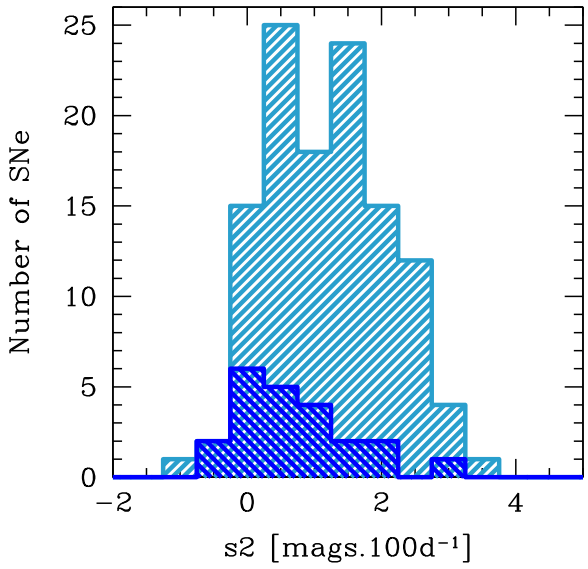

Figure 7. Distribution of the plateau decline s_2 in V band for 117 SNe of our sample. The blue histogram presents the distribution of "s_2" in V band for 22 SNe II used as a new template in SNID.

370 days. One can see the majority (86%) of the spectra were observed between 0 and 100 days since explosion, with a total of 738 spectra. Our earliest spectrum corresponds to SN 2008il at 3 ± 3 days and SN 2008gr at 3 ± 6 days from explosion, while the oldest spectrum is at 363 ± 9 days for SN 1993K. 53% of the spectra were taken prior to 50 days, 3.8% of which were observed before 10 days for 23 SNe. Between ∼30 and 84 days, there are 441 spectra of 114 SNe. There are 115 spectra older than 100 days and 27 older than 200 days, corresponding to 45 and 4 SNe, respectively. The average of spectra as a function of epoch from explosion is 60 days, while its median is 46 days.

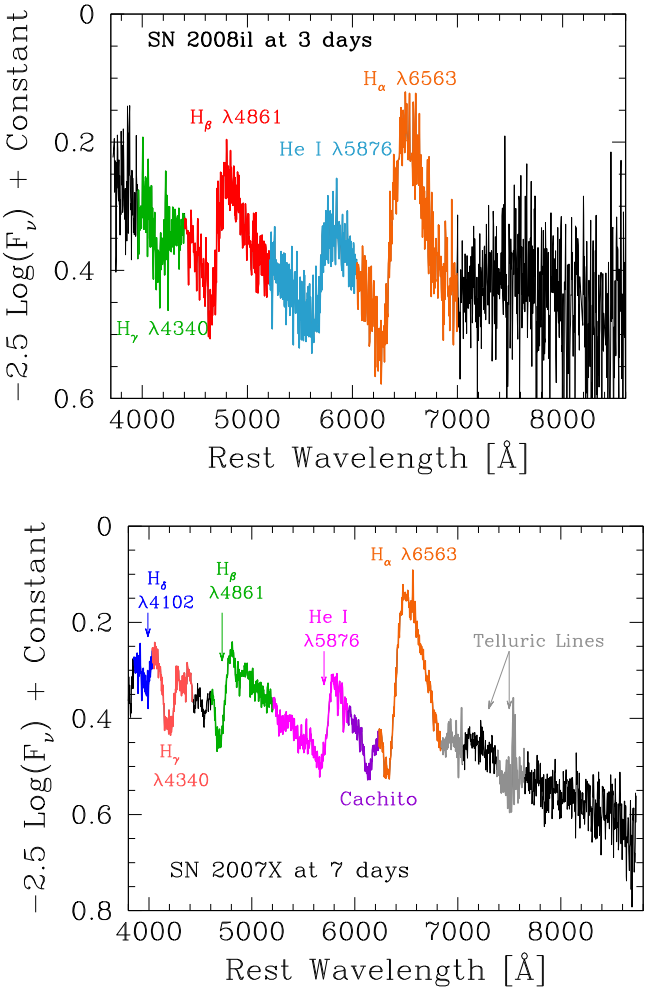

Figure 8. Line identification in the early spectrum of SN 2008il (top) and SN 2007X (bottom).

Figure 6 shows the epoch distribution of the first and last spectrum for each SN in our sample. The majority of SNe have their first spectra within 40 days from explosion. There are 31 SNe with their first spectra around 10 days (the peak of the distribution). On the other hand, the peak of the distribution of the last spectrum is around 100 days. Almost all SNe have their last spectra between 30 and 120 days, i.e., in the photospheric phase. There are 11 SNe with their last spectra occuring after 140 days, while only four SNe (SN 1993K, 2003B, SN 2007it, and SN 2008bk) have their last spectra in the nebular phase ($\geqslant$200 days).

The photometric behavior of our sample in terms of their plateau decline rate (s_2; defined in Anderson et al. 2014b) in the V band is shown in Figure 7. For our sample of 117 SNe II, we measure s_2 values ranging between -0.76 and 3.29 mag 100 day^{-1}. Higher s_2 values mean that the SN has a faster declining light curve. We can see a continuum in the s_2 distribution, which shows that the majority of the SNe (83) have an s_2 value between 0 and 2. There are eight objects with s_2 values smaller than 0, while three SNe show a value larger than 3. The average of s_2 in our sample is 1.20. We are unable to estimate the s_2 value for five SNe, as there is insufficient information from their light curves. The s_2 distribution for the 22 SNe II used as new templates in SNID is also shown in Figure 7. Although the diversity in the SNID templates increased with the inclusion of these SNe, the template distribution is still biased to low s_2 values.

6. Spectral Line Identification

We identified 20 absorption features within our photospheric spectra, in the observed wavelength range of 3800 to 9500 Å. Their identification was performed using the Atomic Spectra Database[26] and theoretical models (e.g., Dessart & Hillier 2005, 2006, 2011). Early spectra exhibit lines of H$_\alpha$ λ6563, H$_\beta$ λ4861, H$_\gamma$ λ4341, H$_\delta$ λ4102, and He I λ5876, with the latter disappearing at $\sim$20–25 days past explosion. An extra absorption component on the blue side of H$_\alpha$ (hereafter "Cachito"[27]) is present in many SNe. That line has previously been attributed to the high velocity (HV) features of hydrogen or Si II λ6533. Figure 8 shows the main lines in early spectra of SNe II at 3 and 7 days from explosion. We can see that SN 2008il shows the Balmer lines and He I, while SN 2007X, in addition to these lines, also shows Cachito on the blue side of H$_\alpha$.

In Figure 9, we label the lines present in the spectra of SNe II during the photospheric phase at 31, 70, and 72 days from explosion. Later than $\sim$15 days, the iron-group lines start to appear and dominate the region between 4000 and 6000 Å. We can see Fe-group blends near λ4554, and between 5200 and 5450 Å (where we refer to the latter as "Fe II blend" throughout the rest of the text). Strong features such as Fe II λ4924, Fe II λ5018, Fe II λ5169, Sc II/Fe II λ5531, the Sc II multiplet λ5663 (hereafter "Sc II M"), Ba II λ6142, Sc II λ6247, O I λ7774, O I λ9263, and the Ca II triplet $\lambda\lambda$8498, 8662 (λ8579) are also present from $\sim$20 days to the end of the plateau. At 31 days, SN 2003hn shows all of these lines, except Ba II, while at 70 and 72 days, SN 2003bn and SN 2007W show all of the lines. Unlike SN 2003bn, SN 2007W shows Cachito and the "Fe line forest."[28] The Fe line forest is visible in a small fraction of SNe from 25–30 days (see the analysis in Section 8). As we can see, there are significant differences between two different SNe at almost the same epoch. Later, we analyze and discuss how these differences can be understood in terms of overall diversity of SN II properties.

In the nebular phase, later than 200 days post-explosion, the forbidden lines [Ca II] $\lambda\lambda$7291, 7323, [O I] $\lambda\lambda$6300, 6364, and [Fe II] λ7155 emerge in the spectra. At this epoch, H$_\alpha$, H$_\beta$, Na I D, the Ca II triplet, O I, and the Fe-group lines between 4800 and 5500 Å, and 6000–6500 Å are also still present. Figure 10 shows a nebular spectrum of SN 2007it at 250 days from explosion.

6.1. The H$_\alpha$ P-Cygni Profile

H$_\alpha$ λ6563 is the dominant spectral feature in SNe II. It is usually used to distinguish different SN types using the initial spectral observation. This line is present from explosion until nebular phases, showing, in the majority of cases, a P-Cygni profile. Although the P-Cygni profile has an absorption and emission component, SNe display a huge diversity in the absorption feature.

[26] http://physics.nist.gov/asd3

[27] Cachito is a Hispanic word that means a small piece of something (like a notch). We use this name to refer to the small absorption components blueward of H$_\alpha$, giving its (until now) previously ambiguous nature.

[28] We label "Fe line forest" to that region around H$_\beta$, where a series of Fe-group (e.g., Fe II λ4629, Sc II λ4670, and Fe II λ4924) absorption lines emerge.

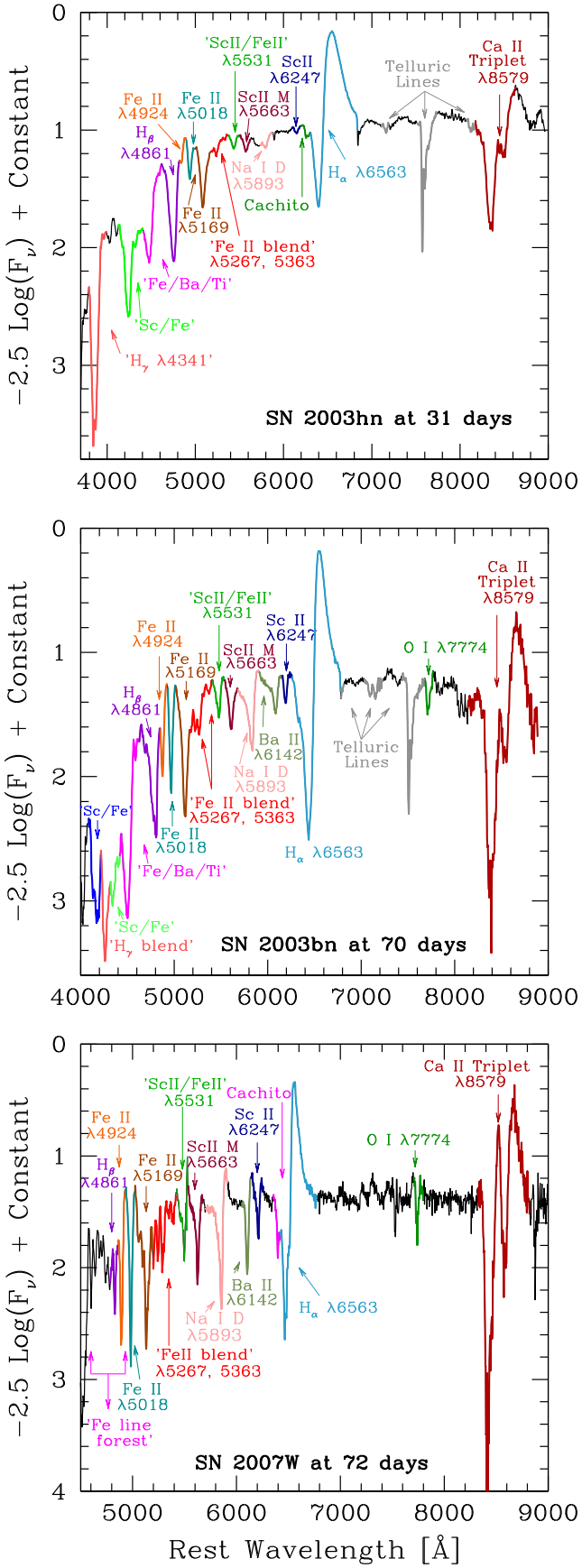

Figure 9. Line identification in the photospheric phase for SNe II 2003hn at 31 days (top), 2003bn at 70 days (middle), and 2007W at 72 days (bottom).

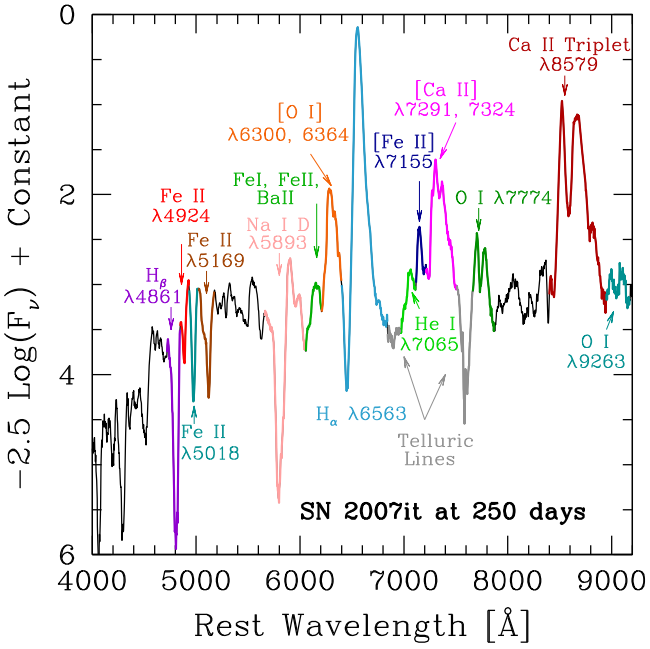

Figure 10. Line identification in the nebular spectrum of SN II 2007it at 250 days from explosion.

Gutiérrez et al. (2014) showed that SNe with little absorption of H_α (smaller absorption to emission (a/e) values) appear to have higher velocities, faster declining light curves, and tend to be more luminous. Here we show that H_α displays a large range of velocities in the photospheric phase, from 9500 to 1500 km s^{-1} at 50 days (see the first two panels in Figure 11, which correspond to the H_α velocity derived from the FWHM of the emission component and from the minimum flux of the absorption, respectively).

The diversity of H_α in the photospheric phase is also observed through the blueshift of the emission peak at early times (Dessart & Hillier 2008; Anderson et al. 2014a) and the boxy profile (Inserra et al. 2011, 2012). The former is associated with differing density distributions of the ejecta, while the latter with an interaction of the ejecta with a dense CSM. In the nebular phase this shift in H_α emission peak has been interpreted as evidence of dust production in the SN ejecta. Despite the fact that this is an important issue in SNe II, only a few studies (e.g., Sahu et al. 2006; Kotak et al. 2009; Fabbri et al. 2011) have focussed on these features.

In Figure 12, we show an example of the evolution of the H_α P-Cygni profile in SN 1992ba. We can see in early phases a normal profile, which evolves to a complicated profile around 65 days. Cachito on the blue side of H_α is present from 65 to 183 days.

6.2. H_β , H_γ, and H_δ Absorption Features

H_β λ4861, H_γ λ4341, and H_δ λ4102 like H_α are present from the first epochs. In earlier phases, these lines show a P-Cygni profile; however, from ∼15 days the spectra only display the absorption component, giving space to Fe-group lines. The range of velocities of H_β, H_γ, and H_δ at 50 days post-explosion vary from 8000 to 1000 km s^{-1} (see Figure 11).

Although H_δ is a common line in SNe II, we do not include a detailed analysis of this line because in many cases the spectra

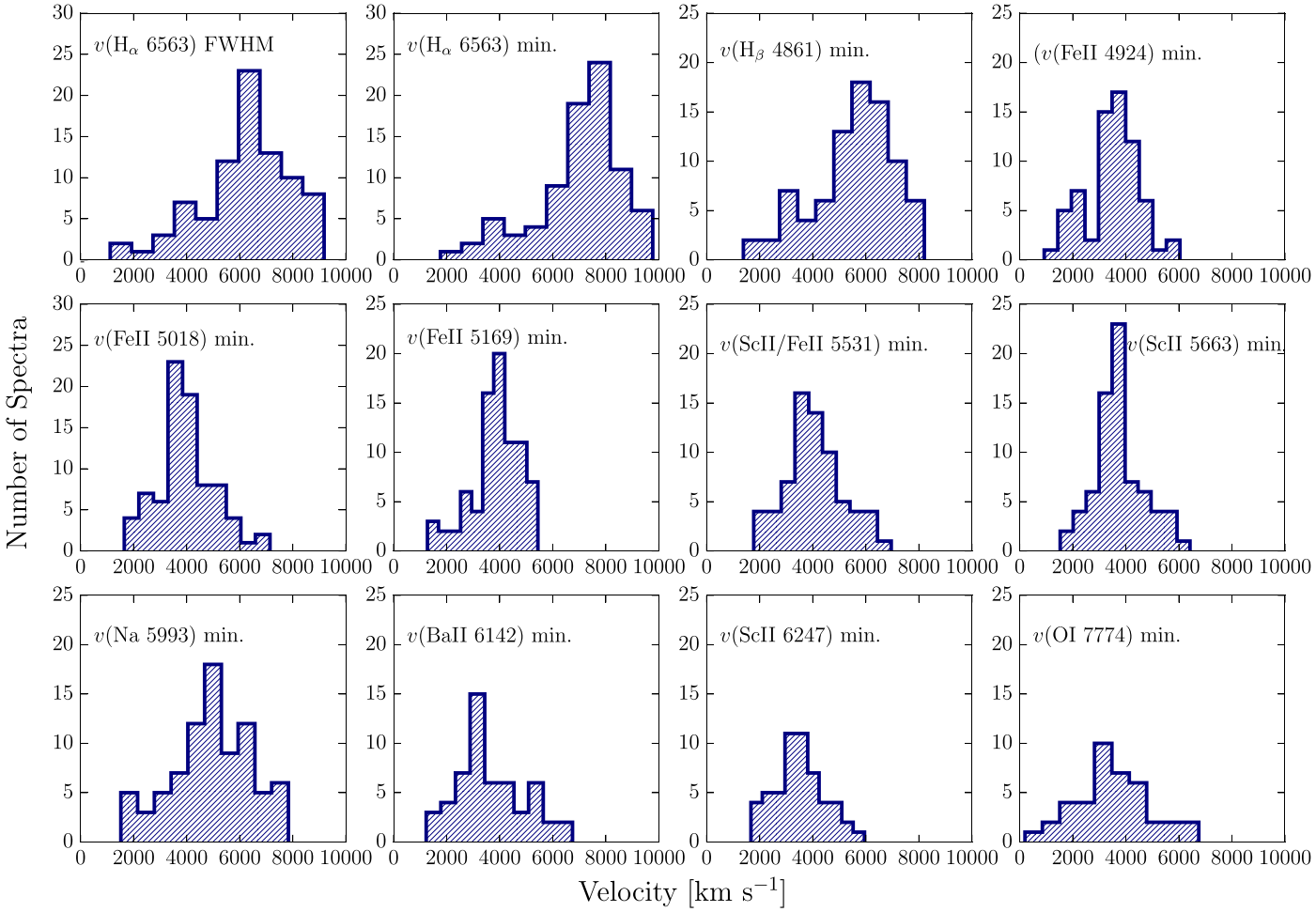

Figure 11. Distribution of the expansion ejecta velocities for 11 optical features at 50 days. The first two panels show the H_α velocity obtained from the FWHM and from the minimum absorption flux. From the third to the twelfth panel are presented the H_β, Fe II λ5018, Fe II λ4924, Fe II λ5169, Sc II/Fe II λ5531, Sc II λ5663, Na I D λ5893, Ba II λ6142, Sc II λ6247, and O I λ7774 velocities obtained from the minimum absorption flux.

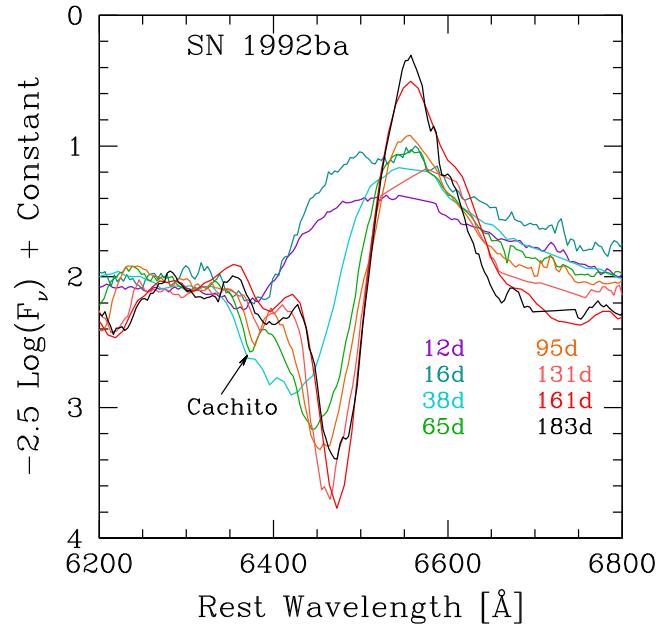

Figure 12. H_α P-Cygni profile evolution in SN 1992ba. The epochs are labeled on the right.

are noisy in the blue part of the spectrum. Besides, like other lines in the blue, this line is blended with Fe-group lines later than 30 days.

Around 30 days from explosion H_γ starts to blend with other lines, such as Ti II and Fe II. Meanwhile, in a few SNe, the H_β absorption feature is surrounded by the Fe line forest. Our later analysis shows that SNe displaying this behavior are generally dimmer and lower velocity events (see Section 8 for more details).

6.3. *He I* λ5876 *and Na I D* λ5893

He I λ5876 is present in very early phases when the temperature of the ejecta is high enough to excite the ground state of helium. As the temperature decreases, the He I line starts to disappear due to low excitation of He I ions (around 15 days; Dessart & Hillier 2010; Roy et al. 2011). At ∼30 days, the Na I D λ5893 absorption feature arises in the spectrum at a similar position where He I was located. This new line evolves with time to a strong P-Cygni profile, displaying velocities between 8000 and 1500 km s^{-1} at 50 days from explosion (Figure 11).

In many SNe II (or indeed SNe of all types), at these wavelengths one often observes narrow absorption features

arising from slow-moving line-of-sight material from the interstellar medium, ISM (or possibly from circumstellar material, CSM). Such material can constrain the amount of foreground reddening suffered by SNe; however, we do not discuss this here.

6.4. Fe-group Lines

When the SN ejecta has cooled sufficiently, Fe II features start to dominate SNe II spectra between 4000 and 6500 Å. The first line that appears is Fe II λ5169 on top of the emission component of H_β. With time Fe II λ5018 and λ4924 emerge between H_β and Fe II λ5169. Fe II λ5169 becomes a Fe II blend later than ~30–40 days. At ~50 days, the 4000–5500 Å region is completely filled with these lines and the continuum is diminished due to Fe II line-blanketing. The H_γ and H_δ absorption features are blended with Fe-group lines, such as Fe II, Ti II, Sc II, and Sr II. Between ~5400 and 6500 Å other metal lines appear in the spectra. Lines such as Sc II/Fe II λ5531, Sc II M, Ba II λ6142, and Sc II λ6247 get stronger with time.

As we can see in Figure 11, the Fe-group lines show a range of velocities between 7000 and 500 km s^{-1} at 50 days. The peak of the distribution of the Fe II group lines velocities is around 4000 km s^{-1}. In the case of Ba II, the peak is lower (around 3000 km s^{-1}).

Although Fe II lines always appear at late phases, few SNe show the iron line forest at 30 days. This feature appears earlier in low velocity/luminosity SNe (see Section 8).

6.5. The Ca II NIR Triplet

The Ca II NIR triplet is a strong feature in the spectra of SNe II. This line appears at ~20–30 days as an absorption feature, but with time it starts to show an emission component. The Ca II NIR triplet results in a blend of λ8498 and λ8542 in the bluer part and a distinct component, λ8662 on the red part. In SNe II with higher velocities these lines are blended producing a broad absorption and emission profile; however, in low velocity SNe, we see two absorption components and one emission in the red part. The velocities of the Ca II NIR triplet range between 9000 and 1000 km s^{-1} at 50 days. In the nebular phase, the Ca II NIR triplet is also present; however, at this epoch, it only exhibits the emission component.

Although in the majority of our spectra we cannot see Ca II H and K λ3945, due to the poor signal-to-noise in this region, this line is present in the photospheric phase of SNe II.

While the Ca II NIR triplet is a prominent feature in SNe II, we do not include its analysis in the subsequent discussion, given that the overlap of lines makes a consistent comparison of velocities and pseudo-equivalent widths (pEWs) difficult.

6.6. O I Lines

The O I $\lambda\lambda$7772, 7775 doublet (hereafter O I λ7774) and O I λ9263 are the oxygen lines in the optical spectra of SNe II. These lines are mainly driven by recombination and they appear when the temperature decreases sufficiently. The O I λ7774 line is relatively strong and emerges around 20 days from explosion; however, in the majority of cases it is contaminated by the telluric A-band absorption (~7600–7630 Å), which hinders detailed analysis. O I λ9263 is weaker and appears one month later than O I λ7774. These lines are present until the nebular phase and their expansion velocity at 50 days post-explosion goes from ~7000 to 500 km s^{-1}, as can be seen in Figure 11.

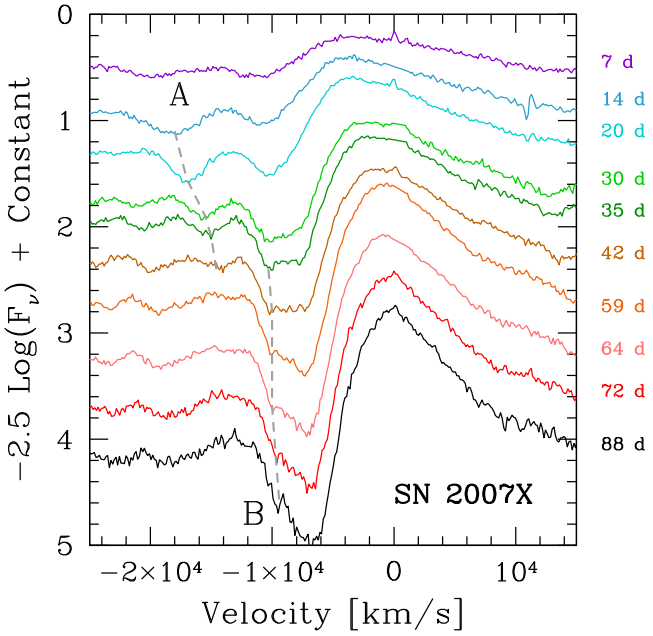

Figure 13. H_α P-Cygni profile of the SN 2007X. The epochs are labeled on the right. The dashed lines indicate the velocities for the A and B features, which we call "Cachito."

6.7. Cachito: Hydrogen High Velocity (HV) Features or the Si II λ6355 Line?

The extra absorption component on the blue side of the H_α P-Cygni profile, called here "Cachito," is seen in early phases in some SNe (e.g., SN 2005cs, Pastorello et al. 2006; SN 1999em, Baron et al. 2000) as well as in the plateau phase (e.g., SN 1999em, Leonard et al. 2002b SN 2007od, Inserra et al. 2011). However, its shape and strength is completely different in the two phases. Baron et al. (2000) assigned the term "complicated P-Cygni profile" to explain the presence of this component on the blue side of the Balmer series. They concluded that these features are due to velocity structures in the expanding ejecta of the SNe II. A few years later, Pooley et al. (2002) and Chugai et al. (2007) argued that this extra component might originate from ejecta—circumstellar (CS) interactions, while Pastorello et al. (2006) earmarked this feature as Si II λ6355.

In general, Cachito appears around 5–7 days between 6100 and 6300 Å, and disappears at ~35 days after explosion. Later than 40 days, the Cachito feature emerges closer to H_α (between 6250 and 6450 Å) and it can be seen until 100–120 days. Figure 13 shows this component in SN 2007X. In early phases, this feature is marked with letter A and later with letter B. If attributed to H_α the derived velocities are 18,000 and 10,000 km s^{-1}, respectively. A detailed analysis of this feature is presented in Section 8.4.

6.8. Nebular Features

As mentioned above, H_α, H_β, the Ca II NIR triplet, Na ID, O I, and Fe II are also present in the nebular phase (later than

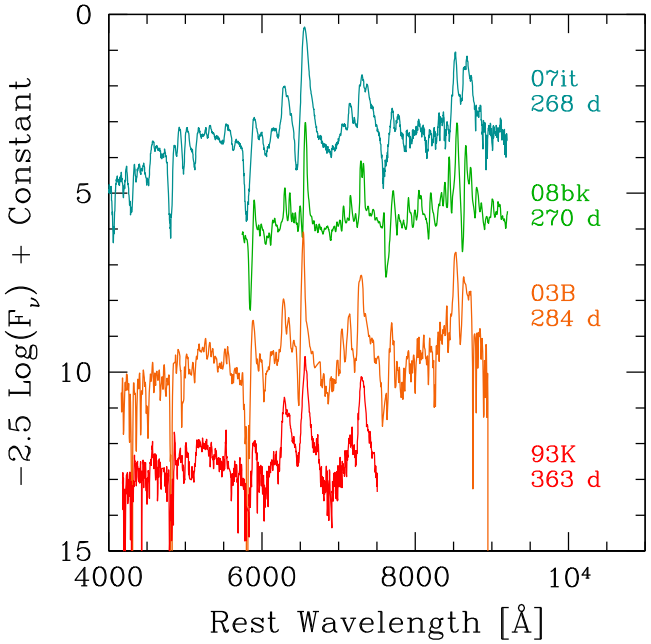

Figure 14. Nebular spectra of seven different SNe of our sample. The spectra are organized according to epoch.

200 days since explosion); however, in the case of the Ca II NIR triplet, its appearance changes, passing from absorption and emission components to only emission components when the nebular phase starts. The rest of the lines have the same behavior but at much later epochs. The emergence of forbidden emission lines signifies that the spectrum is now forming in regions of low density. At this phase, the ejecta has become transparent, allowing us to peer into the inner layers of the rapidly expanding ejecta. Lines such as [Ca II] $\lambda\lambda$7291, 7323, [O I] $\lambda\lambda$6300, 6364, and H_α are the strongest features visible in the spectra.

The [O I] doublet observed at nebular times is one of the most important diagnostic lines of the helium-core mass (Fransson & Chevalier 1987; Jerkstrand et al. 2012). Usually the doublet is blended; however, in SNe with low velocities these lines can be resolved (see, e.g., SN 2008bk). On the other hand, [Fe II] λ7155 is easily detectable, but in most cases it is blended with [Ca II] $\lambda\lambda$7291, 7323, and He I λ7065, which may hinder their analysis. In Figure 14, we can see the diversity found in the nebular spectra in our sample.

7. Spectral Measurements

As discussed previously, SNe II spectra evolve from having a blue continuum with a few lines (Balmer series and He I) to redder spectra with many lines: Fe II, Ca II, Na I D, Sc II, Ba II, and O I. To analyze the spectral properties of SNe II, we measure the expansion velocities and pEWs of 11 features in the photospheric phase (see in Table 3 the features used), the ratio of absorption to emission (a/e) of H_α P-Cygni profile before 120 days, and the velocity decline rate of H_β.

Table 3
Spectral Features Used for the Statistical Analysis in the Photospheric and Nebular Phases

Feature Name	Rest Wavelength[a] (Å)	Blueward Limit Range[b] (Å)	Redward Limit Range[b] (Å)
H_α	6563	6000–6300	6900–7100
H_β	4861	4400–4700	4800–4900
Fe II	4924	4800–4900	4900–4950
Fe II	5018	4900–4500	5000–5050
Fe II	5169	5000–5050	5100–5300
Na I	5893	5500–6000	5800–6000
Sc II	5531	5400–5450	5500–5550
Sc II/Fe II	5663	5500–5550	5600–5700
Ba II	6142	6000–6050	6100–6150
Sc II	6247	6150–6170	6250–6270
O I	7774	7630–7650	7750–7780

Notes.
[a] The rest wavelengths are weighted averages of the strongest spectral lines that give rise to each absorption feature.
[b] These limits are necessary in order to account for variations in spectral feature width and expansion velocity among SNe.

7.1. Expansion Ejecta Velocities

The expansion velocities of the ejecta are commonly measured from the minimum flux of the absorption component of the P-Cygni line profile. Using the Doppler relativistic equation and the rest wavelength of each line, we can derive the velocity. To obtain the position of the minimum line flux (in wavelength), a Gaussian fitting was employed, which was performed with IRAF, using the *splot* package. As the absorption component presents a wide diversity (e.g., asymmetries, flat shape, extra absorption components), we repeat the process many times (changing the pseudo-continuum), and the mean of the measurements was taken as the minimum flux wavelength. As our measurement error, we take the standard deviation on the measurements. This error is added in quadrature to errors arising from the spectral resolution of our observations (measured in Å and converted to kilometers per second) and from peculiar velocities of host galaxies with respect to the Hubble flow (200 km s^{-1}). This means that, in addition to the standard deviation error, which realizes the width of the line and S/N, we take into account the spectral resolution, which, in our case, is the most dominant parameter to determine the error.

The particular case of the H_α velocity was explored in Gutiérrez et al. (2014). Due to the difficulty of measuring the minimum flux in a few SNe with little or extremely weak absorption components, we derive the expansion velocity of H_α using both the minimum flux of the absorption component and the full width at half maximum (FWHM) of the emission line.

In the case of O I λ 7774, where the telluric lines can affect our measurement of its absorption minimum, we only use SNe with a clear separation between the two features. This means that the number of SNe with O I measurements is significantly smaller (only 47 SNe) compared to the other measured features.

7.2. Velocity Decline Rate

To calculate the time derivative of the expansion velocity in SNe II, we select the H_β absorption line. It is present from the

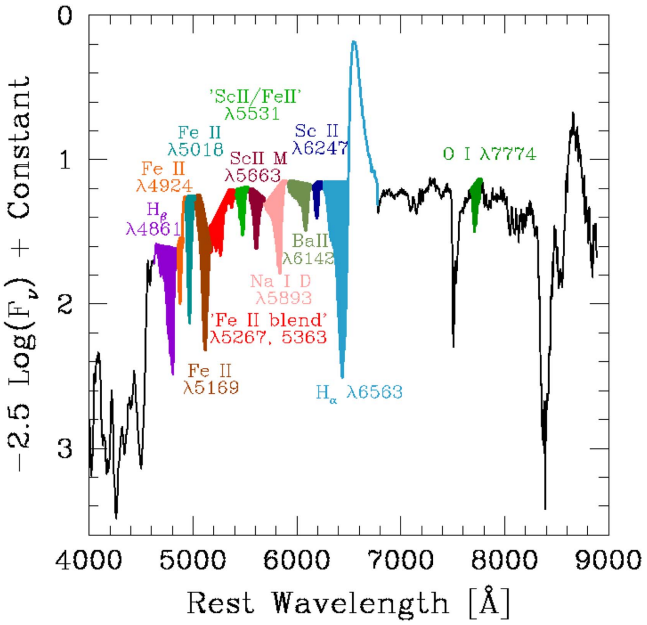

Figure 15. Examples of pEWs used in this work for 11 features in the photospheric phase of SN 2003bn (at 70 days).

early spectra, it is easy to identify and it is relatively isolated. To quantitatively analyze our sample, we introduce the $\Delta v(\mathrm{H}_\beta)$ as the mean velocity decline rate in a fixed phase range $[t_0,t_1]$: $\Delta v(\mathrm{H}_\beta) = \frac{\Delta v_{\mathrm{abs}}}{\Delta t} = \frac{v_{\mathrm{abs}}(t_1) - v_{\mathrm{abs}}(t_0)}{t_1 - t_0}$.

This parameter was measured over the interval [+15, +30] d, [+15, +50] d, [+30, +50] d, [+30, +80] d, and [+50, +80] d.

7.3. Pseudo-equivalent Widths

To quantify the spectral properties of SNe II, another avenue for investigation is the measurement and characterization of spectral line pEWs. The prefix "pseudo" is used to indicate that the reference continuum level adopted does not represent the true underlying continuum level of the SN, given that in many regions the spectrum is formed from a superposition of many spectral lines. The pEW basically defines the strength of any given line (with respect to the pseudo-continuum) at any given time. The simplest and most often used method is to draw a straight line across the absorption feature to mimic the continuum flux. Figure 15 shows an example of this technique applied to SN 2003bn. We do not include analysis of spectral lines where it is difficult to define the continuum level, due to complicated line morphology, such as significant blending between lines. For example, later than 20–25 days, all absorption features bluer than H_β are produced by blends of Fe-group lines plus other strong lines, such as Ca II H & K and H_γ. On the other hand, the Ca II NIR triplet $\lambda\lambda$8498, 8662 shows a profile that depends on the SN velocity (higher velocity SNe show a single broad absorption, while low velocity SNe show two absorption characteristics). These attributes make a consistent analysis between SNe difficult, and therefore we do not include this line in our analysis.

We measure the ratio of absorption to emission (a/e) in H_α until 120 days. In the same way, the pEWs of the absorption lines are measured, we evaluate the pEWs for the emission in H_α, thus we have: $a/e = \frac{p\mathrm{EW}(H_{\alpha(\mathrm{abs})})}{p\mathrm{EW}(H_{\alpha(\mathrm{emis})})}$.

8. Line Evolution Analysis

Here we study the time of appearance of different lines within different SNe and make a comparison of those SNe with/without specific lines at different epochs. For all lines included in our analysis, we search for their presence in each observed spectrum. Then, at any given epoch, we obtain the percentage of SNe that display each line. This enables an analysis of the overall line evolution of our sample and whether the speed of this evolution changes between different SNe of different light curve, spectral, and environment (metallicity) characteristics.

In Figure 16 we show the percentage of SNe displaying specific spectral features as a function of time. As discussed previously, H_α and H_β are permanently present in all the SNe II spectra from the first days, so we do not include them in the plot. We can see the following.

1. The feature located in the position of He I/Na I D is visible in all epochs; however, around 15–25 days, fewer SNe show the line with respect to either the earlier or later spectrum. We suggest that in this epoch the transition from He I to Na I D happens. Therefore, after 30 days, we refer to this line as Na I D. It is present in 96% of the spectra from ∼35 days. Later than 43 days, it is present in all spectra.
2. The Ca II NIR triplet is present in 50% of the sample at ∼20 days. Before 20 days, it is present in ∼12% of the sample, while later than 25 days it is visible in almost all the sample, but with one exception at 38 days. The latter is SN 2009aj, which shows signs of CS interaction in the early phases.
3. H_γ blend with Fe-group lines starts at ∼20 days from explosion, growing dramatically at 35–45 days. Only one spectrum at ∼46 days does not show the blend (SN 2008bp).
4. The Fe-group lines start to appear at around 10 days (see Figure 16). The first line that emerges is Fe II λ5169. We can see that few SNe exhibit the absorption feature before 15 days; however, later at 15 days, around 50% of SNe show the line and at 30 days all objects have it. The next line that arises is Fe II λ5018. This line is seen from 15 days, being present in all SNe later than 40 days. Meanwhile, Fe II λ4924 is seen in one spectrum at 13 days (SN 2008br). From 30 days, it is visible in more than 50% of the spectra. The Sc II/Fe II λ5531, Sc II multiplet λ5668, Ba II λ6142, and Sc II λ6246 are detectable later than 30 days. The emergence of the Sc II/Fe II λ5531 and Sc II multiplet λ5668 happens at similar epochs, as well as Ba II λ6142 and Sc II λ6246.

In order to further understand the differences in line-strength evolution of SNe II, we separate the sample into those SNe that do/do not display a certain spectral feature at some specific epoch. We then investigate whether these different samples also display differences in their light curves and spectra. This is done by using the Kolmogorov–Smirnov (KS) test. Presented in Table 4 are all the results obtained with the KS test: SNe with/without a given line as a function of a/e and H_α velocity at $t_{\mathrm{tran}+10}$,[29] M_{max}, s_2, and metallicity (derived from the ratio of

[29] $t_{\mathrm{tran}+10}$ is defined as the transition time (in $V-band$) between the initial and the plateau decline, plus 10 days. In other words, t_{tran} marks the start of the recombination phase. (See A14 and Gutiérrez et al. 2014 for more details.)

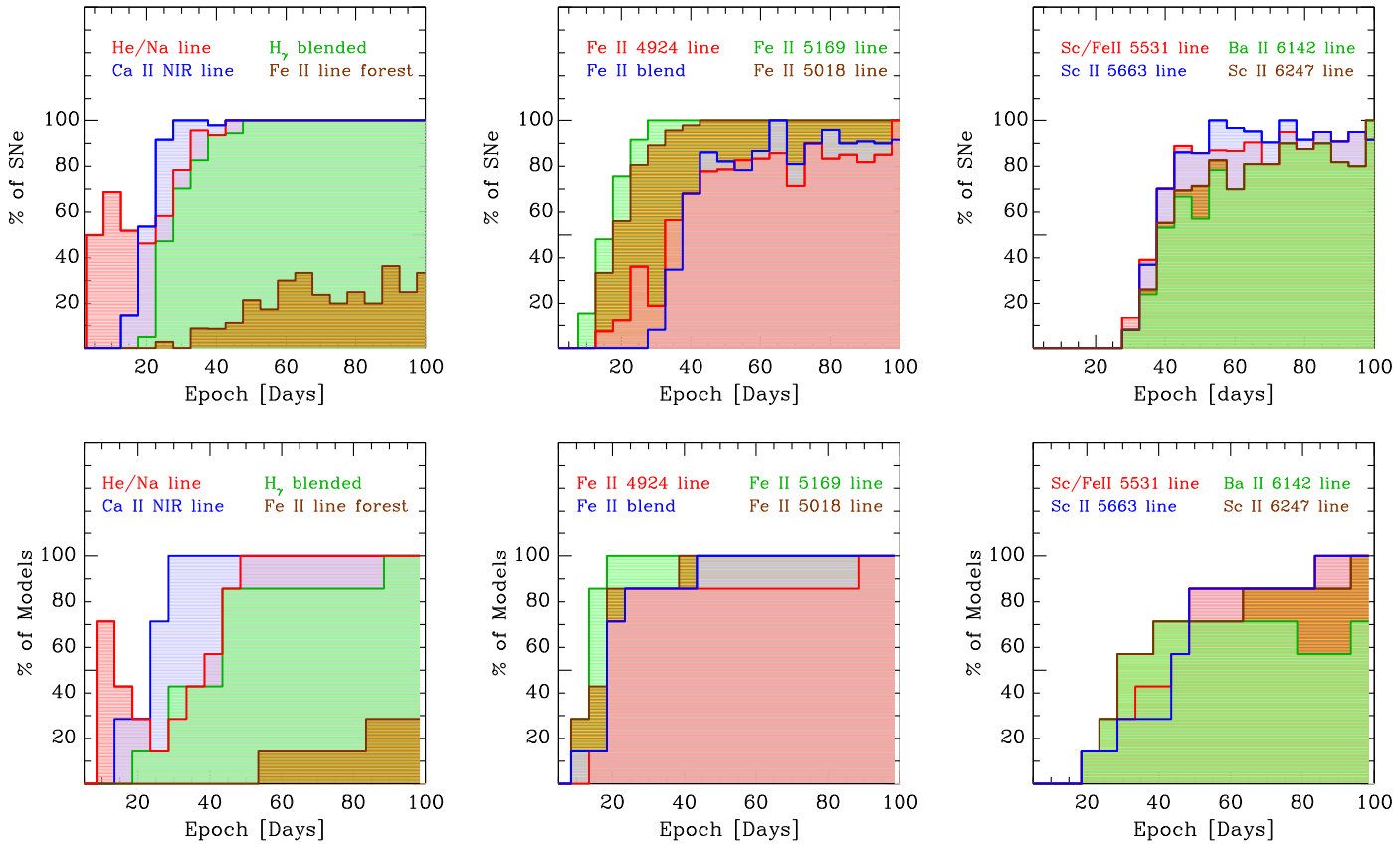

Figure 16. Appearance of different lines in SNe II between explosion and 100 days. Top: from the observed spectra. Bottom: from synthetic spectra (see more details in Table 5).

Table 4
KS-test Values

Feature name	$v(H_\alpha)$	a/e	M_{max}	s_2	M13 N2	Epoch (days)
Fe II line forest	5.19	9.80	**2.17**	3.73×10^{-4}	**4.38**	0–100
H_γ blended	29.75	58.33	31.21	55.32	16.10	23–27
He I 5876	18.62	**1.91**	30.94	25.73	46.18	18–22
Ca II IR triplet	87.73	91.97	94.47	53.30	98.82	18–22
Fe II 4924	**2.82**	16.84	**1.09**	**4.80**	99.40	28–32
Fe II 5018	15.68	90.80	99.02	68.84	61.53	18–22
Fe II 5169	60.76	35.15	74.88	50.83	20.30	13–17
Fe II multiplet	21.38	26.75	**1.00**	**0.25**	99.28	33–37
Sc II/Fe II 5531	75.60	89.60	30.34	45.20	**1.84**	38–42
Sc II multiplet 5663	63.54	63.54	30.34	80.10	**0.79**	38–42
Ba II 6142	45.75	83.58	**1.90**	57.43	**1.29**	38–42
Sc II 6247	45.76	83.58	**1.89**	57.42	**0.52**	38–42

Note. Percentage obtained using a KS test to verify if two distributions (with and without each line) are drawn from the same parent population as a function of $v(H_\alpha)$, a/e, M_{max}, s_2, and M13 N2 in an particular epoch. This epoch is shown in the last column of the table. Values lower than 10% are presented in bold.

H_α to [N II] λ6583, henceforth M13 N2 diagnostic; Marino et al. 2013) in a particular epoch. The values of the first four parameters can be found in Table 1 in Gutiérrez et al. (2014), while the metallicity information was obtained from Anderson et al. (2016). We find the following.

1. SNe II that never display the Fe II line forest are distinctly different from those that do display the feature. Specifically, those that do show this feature have slow declining light curves (smaller s_2), are dimmer, and are found to explode in higher metallicity regions within their hosts (see Table 4 for exact statistics).
2. There is less than a 2% probability that those SNe II, where the He I line is detected between 18 and 22 days post-explosion, arise from the same underlying parent population of a/e. This suggests that temperature differences between SNe II affect the morphology of the H_α feature.

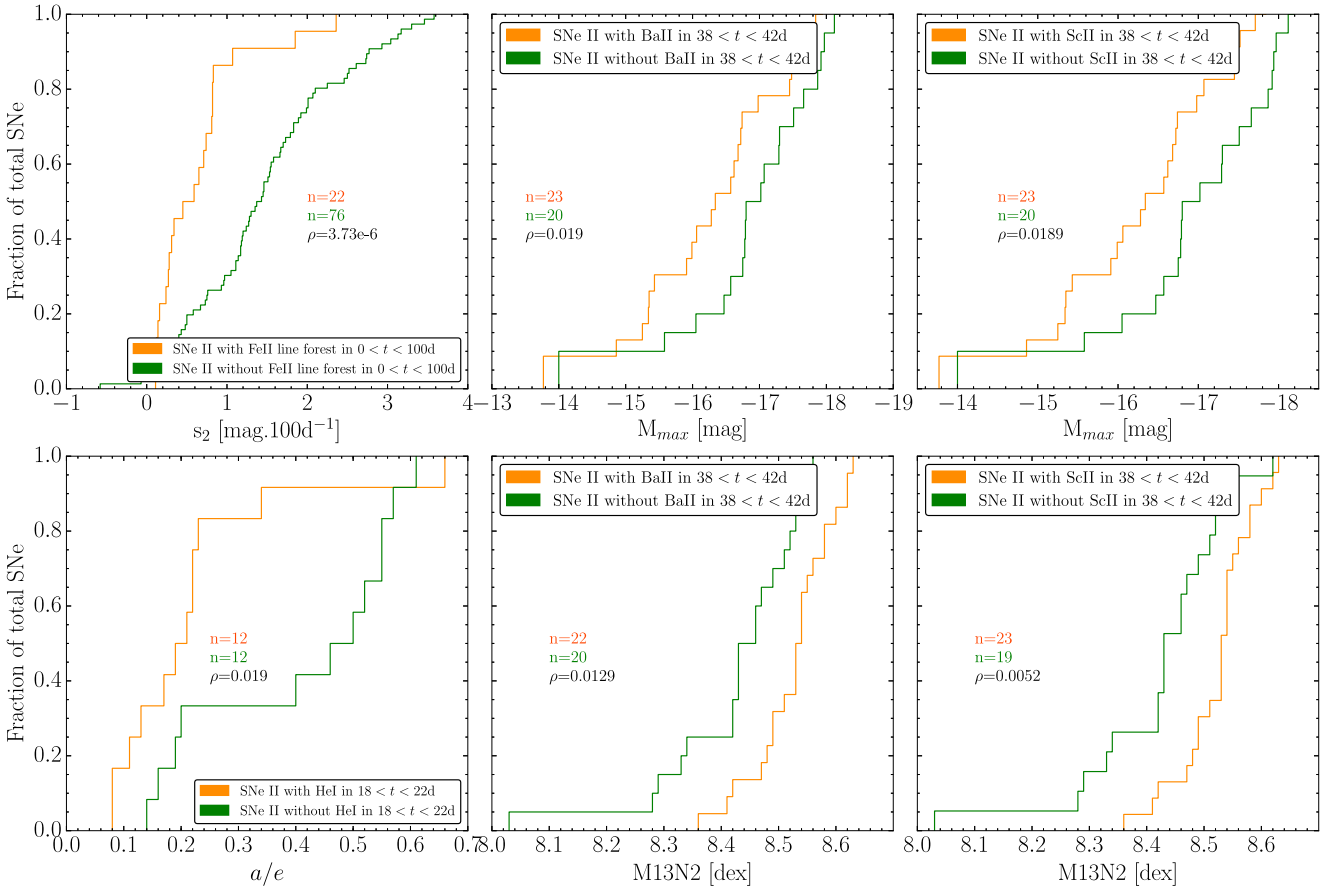

Figure 17. Cumulative distributions of each SN with/without different lines as a function of spectral and photometric and environment properties. First panel: SNe with/without Fe II line forest between explosion and 100 days as a function of s_2; second panel: SNe with/without Ba II between 38 and 42 days as a function of $M_{\rm max}$; third panel: SNe with/without Sc II between 38 and 42 days as a function of $M_{\rm max}$; fourth panel: SNe with/without He I between 18 and 22 days as a function of a/e; fifth panel: SNe with/without Ba II between 38 and 42 days as a function of M13 N2 diagnostic; sixth panel: SNe with/without Sc II between 38 and 42 days as a function of M13 N2 diagnostic.

3. Ba II λ6142 and Sc II λ6247 are both more likely to be detected at around 40 days post-explosion in dimmer SNe II, with only a 2% probability that the two populations (with and without these lines) are drawn from the same $M_{\rm max}$ distribution.
4. Finally, when splitting the SNe II sample into those that do and do not display Sc II/Fe II λ5531, Sc II multiplet λ5668, Ba II λ6142, and Sc II λ6247 at around 40 days post-explosion, we find that there is only around a 1% probability that the two samples are drawn from the same distribution of metallicity: those SNe that do not display these lines at this epoch are found to generally explode in regions of lower metallicity within their hosts.

Figure 17 presents the cumulative distributions of the most significative findings obtained with the KS-test analysis.

This analysis was also performed with synthetic spectra for seven different models from Dessart et al. (2013). Four models (m15z2m3, m15z8m3, m15z8m3, and m15z4m2) show differences in the metallicity, while the rest of the properties are almost the same. The three remaining models have the same metallicity (solar metallicity); however, the other parameters are different: m15mlt1 has a bigger radius (twice times the radius of the two other models), m15mlt3 has higher kinetic energy, while m12mlt3 displays a smaller final progenitor mass and less kinetic energy (1/5 $E_{\rm kin}$ compared with the other models). More details are shown in Table 5.

Table 5
Model properties

Model	Z ($Z_\odot$)	$M_{\rm final}$ ($M_\odot$)	R_* ($R_\odot$)	$E_{\rm kin}$ (B)
m15z2m3	0.1	14.92	524	1.35
m15z8m3	0.4	14.76	611	1.27
m15z8m3	1.0	14.09	768	1.27
m15z4m2	2.0	12.60	804	1.24
m15mlt1	1.0	14.01	1107	1.24
m15mlt3	1.0	14.08	501	1.34
m12mlt3	1.0	10.50	500	0.25

Note. Summary of model properties used in this work.
Columns: (1) model name; (2) metallicity; (3) final progenitor mass; (4) progenitor radius; (5) kinetic energy.

In general, the synthetic spectra show the same behavior (in relation to the appearance of the lines) as observed spectra. However, some differences are found, the majority of which

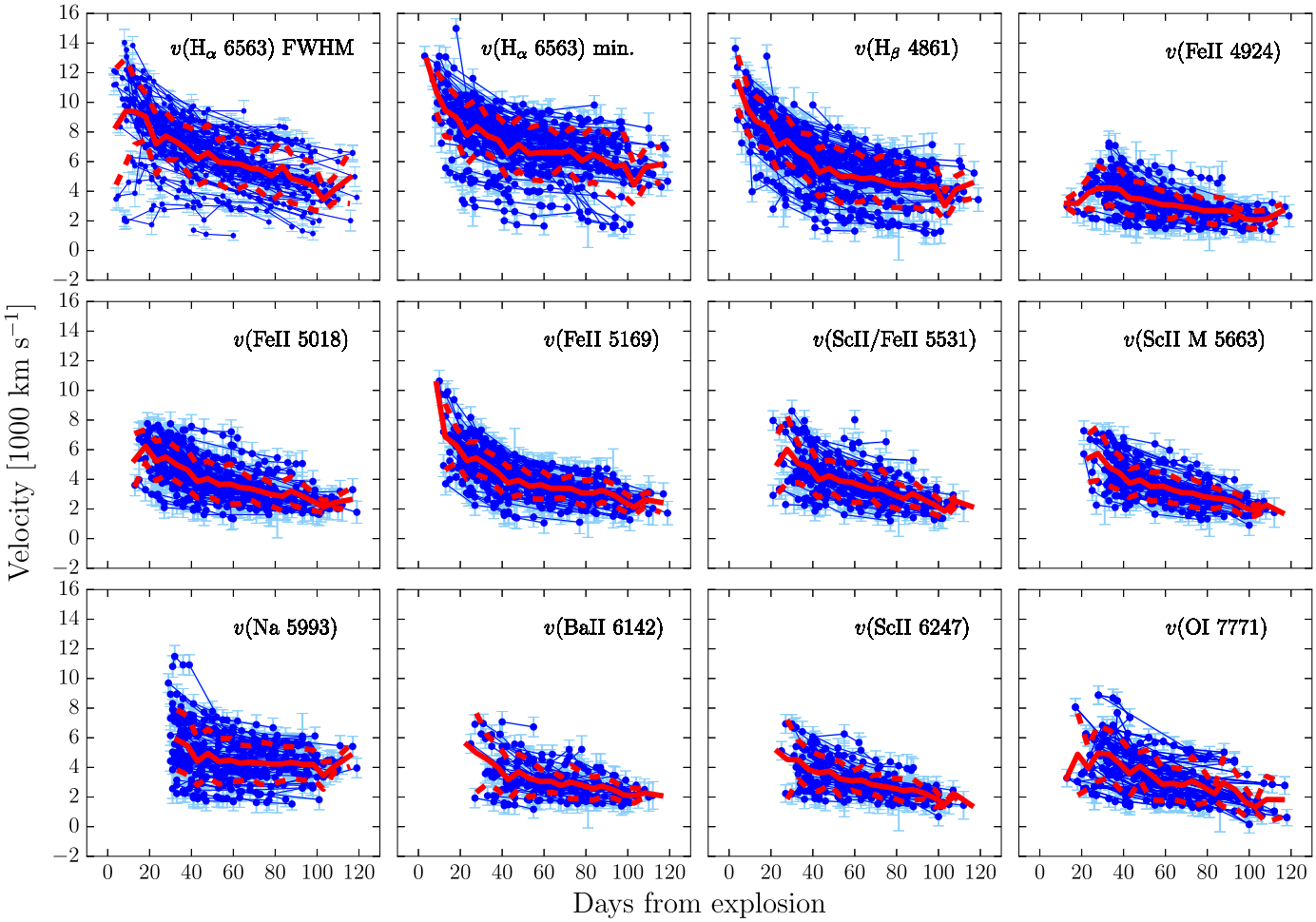

Figure 18. Expansion velocity evolution for H_α (from the FWHM of emission and the minimum flux absorption), H_β, Fe II λ4924, Fe II λ5018, Fe II λ5169, Sc II/Fe II, Sc II multiplet, Na I D, Ba II, Sc II, and O I from explosion to 120 days. The red solid line represents the mean velocity within each time bin, while the dashed red lines indicate the standard deviation. Table 8 presents these values.

are probably related with the low area of parameter space covered by the models that currently exist as compared to the parameter space covered by real events. The transition between He I to Na I D is more evident, and it happens between 18 and 40 days. Although the transition in the models is unambiguously identified by knowing the optical depth of specific lines, in these synthetic spectra, this happens a little bit later than in observed ones. This suggests that the temperature in specific models stays higher for a longer time than the average for observed SNe II. It is also likely that the observed SNe II span a smaller range in progenitor metallicity than the models (that go down to a tenth solar). The Na I D is visible in 100% of the sample after 50 days, only 5 days later than the observed spectra. Ca II shows the same behavior in both synthetic and observed spectra; however, H_γ is blended in all of the sample later than 90 days, unlike the observed spectra that show it from 45 days. On the other hand, the Fe II line forest is visible from 55 days, in contrast to the observed spectra that show this characteristic from 30 days. This behavior is only present in the spectra of the higher metallicity model (two times solar) and in the lower explosion energy model. The iron lines (Fe II λ4924, Fe II λ5018, Fe II λ5169, and the Fe II blended) are present from $\sim$10 days. Fe II λ5169 is visible in 50% of the spectra at $\sim$15

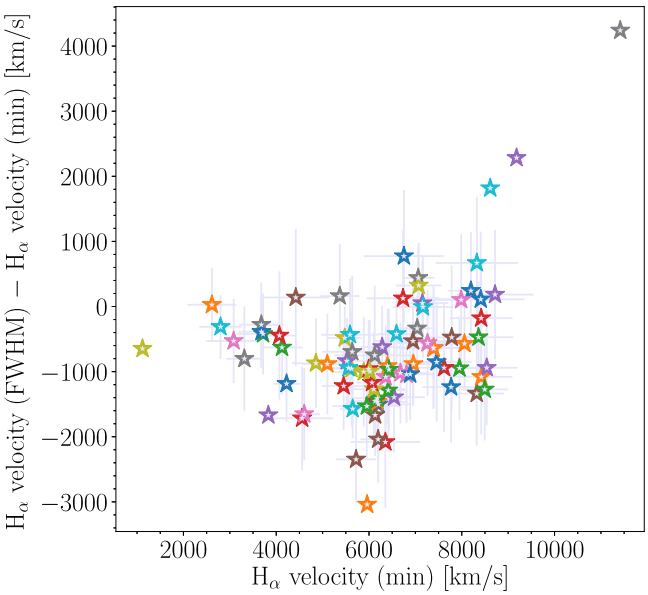

Figure 19. Shifts of the H_α velocity obtained from the FWHM of the emission and from the minimum of the absorption at 50 days post-explosion.

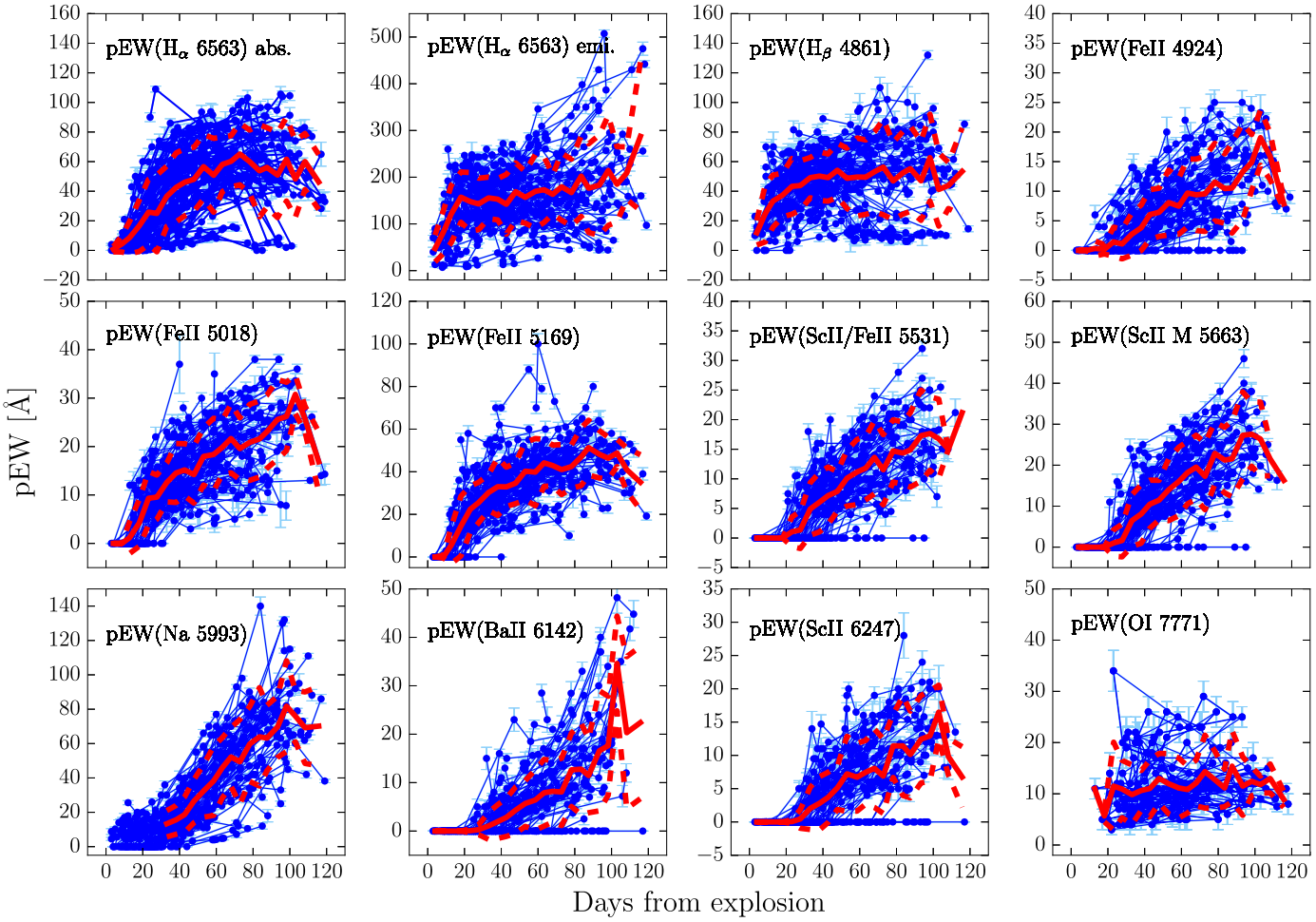

Figure 20. pEWs evolution for H_α absorption, H_α emission, H_β, Fe II λ4924, Fe II λ5018, Fe II λ5169, Sc II/Fe II, Sc II multiplet, Na I D, Ba II, Sc II, and O I from explosion to 120 days. The red solid line represents the mean pEW within each time bin, while the dashed red lines indicate the standard deviation. Table 9 presents these values.

days, while Fe II λ4924 is only visible in ~10%. From 20 days, Fe II λ5169 is present in all the synthetic spectra, 10 days earlier than in the observed ones. The behavior of Fe II λ5018 is similar in both synthetic and observed spectra, whereas Fe II λ4924 starts faster in the models and it is visible in 85% of the spectra from 30 days. We can see differences in the Fe II blend, which is visible in 100% of the sample from 50 days in the models; however, in the observed spectra that never happens. More differences are also appreciable between models and observation in Sc II/Fe II λ5531, the Sc II multiplet λ5668, Ba II λ6142, and Sc II λ6246. These lines in models arise from 20 days, but in the observations it occurs from 38 to 40 days. Nevertheless, the evolution of the distribution is similar from 50 days. In conclusion, while in general the models produce a time evolution of spectral lines that is quite similar to the observations—supporting the robustness of the models—we observe small differences, suggesting a wider range of explosion and progenitor properties is required to explain the full diversity of observed SNe II.

8.1. Expansion Velocity Evolution

Figure 18 shows the velocity evolution of 11 spectral features as a function of time. The first two panels of the plot show the expansion velocity of the H_α feature: on the left, the velocity derived from the FWHM and on the right that derived from the minimum absorption flux. As we can see, the behavior is similar; however, the velocity obtained from the minimum absorption flux is offset between 10% and 20% to higher velocities. Figure 19 shows this shift at 50 days. Velocities obtained from the minimum absorption flux are higher around ~1000 km s^{-1}. However, it is possible to see few SNe (with higher H_α velocities) showing higher values from the FWHM. Using the Pearson correlation test, we find a weak correlation, with a value of $\rho = 0.37$. SNe II with narrower emission components display a larger offset between the velocity from the FWHM and that from the minimum of the absorption. In contrast, those SNe II displaying the highest FWHM velocities present comparatively lower minimum absorption velocities. We note also the presence of two outliers (extreme cases, the lowest and highest value). Figure 11 shows the velocity distribution for the 11 features at 50 days post-explosion. We can see that H_α shows higher velocities than the other lines, followed by H_β. The lowest velocities are presented by the iron-group lines. In Figure 18, it is possible to see that the H_β expansion velocity shows the typical evolution for a homologous expansion and like H_α, it is possible to see it from early phases. The iron lines display lower velocities than the Balmer

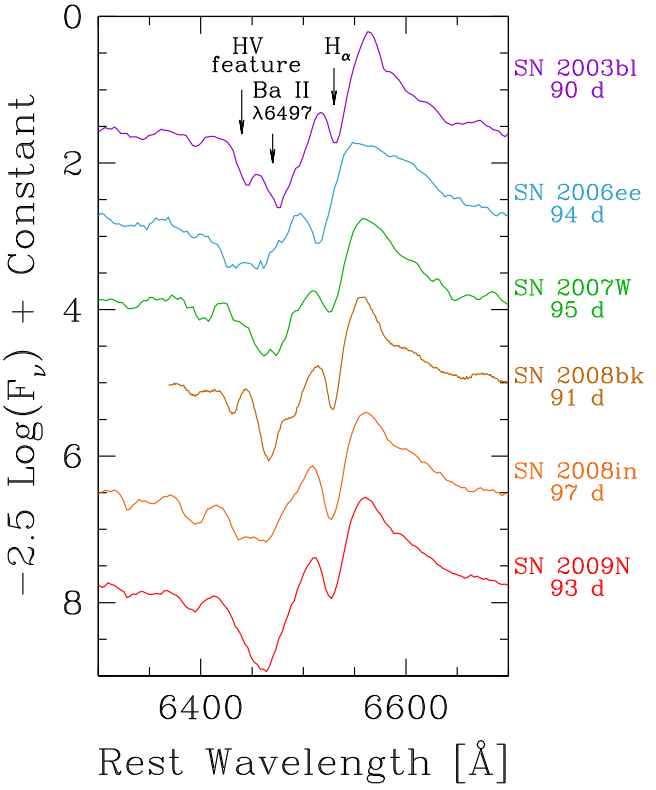

Figure 21. H_α P-Cygni profile of low and intermediate velocity SNe II: 2003bl, 2006ee, 2007W, 2008bk, 2008in, and 2009N around 95 days post-explosion.

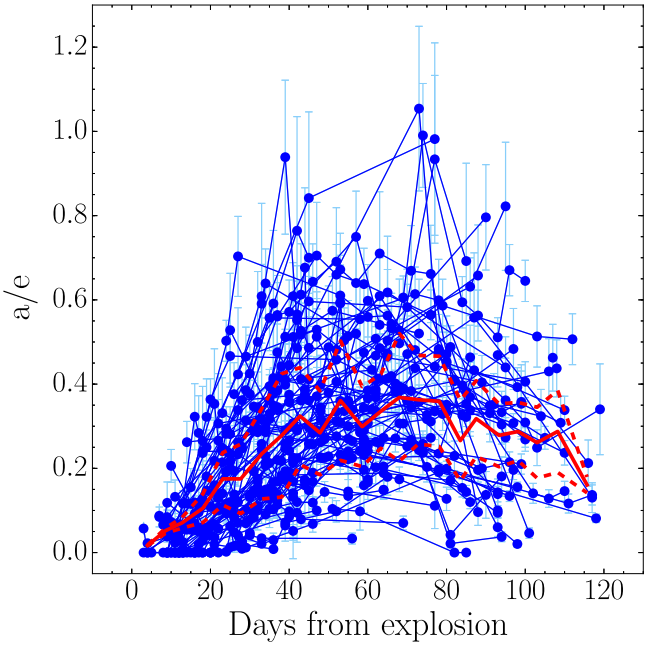

Figure 22. Evolution of the ratio absorption to emission (a/e) of H_α between explosion and 120 days.

lines. So, the highest velocity in SNe II is found in H_α, which implies that it is formed in the outer layers of the SN ejecta. Meanwhile, based on the lower velocities, the iron-group lines form in the inner part, closer to the photosphere. The O I line does not show a strong evolution. As we can see, its velocity evolution is almost flat.

The lowest velocities are found in SN 2008bm, SN 2009aj, and SN 2009au. However, these SNe are distinct from the rest of the population. Unlike subluminous SNe II (such as SN 2008bk and SN 1999br)—that also display low expansion velocities—these events are relatively bright. They also show early signs of CS interactions, e.g., narrow emission lines. By contrast, SN 2007ab, SN 2008if, and SN 2005Z have the largest velocities.

8.2. Velocity Decline Rate of H_β Analysis

The velocity decline rate of SNe II, denoted as $\Delta v(H_\beta)$, has not been previously analyzed. We estimate $\Delta v(H_\beta)$ in five different epochs (outlined above) to understand their behavior. We find that SNe with a higher decline rate at early times continue to show such behavior at later times. The median velocity decline rate for our sample between 15 and 30 days is 105 km s^{-1} day^{-1}, while between 50 and 80 days is 29 km s^{-1} day^{-1}. These results show an evident decrease in the velocity decline rate at two different intervals, which is consitent with homologous expansion.

8.3. pEWs Evolution

The temporal evolution of pEWs for each of the 11 spectral features is shown in Figure 20. In general, the pEWs increase quickly in the first one to two months then level off. The first two panels show the pEW evolution of H_α. On the left is displayed the absorption, while on the right the emission component. The absorption component monotonically increases from 0, increasing to ∼100 Å; however, in a few SNe its evolution is different: from 70 days, the pEW decreases significantly. This behavior is observed in low and intermediate velocity SNe (e.g., SN 2003bl, SN 2006ee, SN 2007W, SN 2008bk, SN 2008in, and SN 2009N). Generally, these SNe show a very narrow H_α P-cygni profile, and at around 70 days from explosion Ba II λ6497 appears in the spectra as a dominant feature (see Roy et al. 2011; Lisakov et al. 2017 for more details). In Figure 21, we can see the H_α P-Cygni profile with the presence of Ba II λ6497, and the HV feature of hydrogen line (see Section 8.4 for more details) on the blue side of Ba II.

Figure 20 also shows the H_α emission component evolution. An increment in the pEW in the majority of SNe is appreciable. There are a couple cases (e.g., SN 2006Y), displaying a quasi-constant evolution. The range of pEW of H_α emission goes up 400 Å. In the case of H_β, we can see that from 60 days there are few SNe with low pEW values, which show a quasi-constant evolution. SNe with this behavior are those that show the Fe II line forest. The remaining SNe show an increase. The pEWs of iron-group lines grow with time; however, there is a group of SNe with pEW = 0. This indicates that some specific SNe do not have the line yet. For Sc II/Fe II, the Sc II multiplet, Ba II, and Sc II, this is more obvious. On the other hand, the O I shows a quasi-constant behavior and Na I D shows a steady increase. Comparing the values, we can see that the absorption of H_α, H_β,

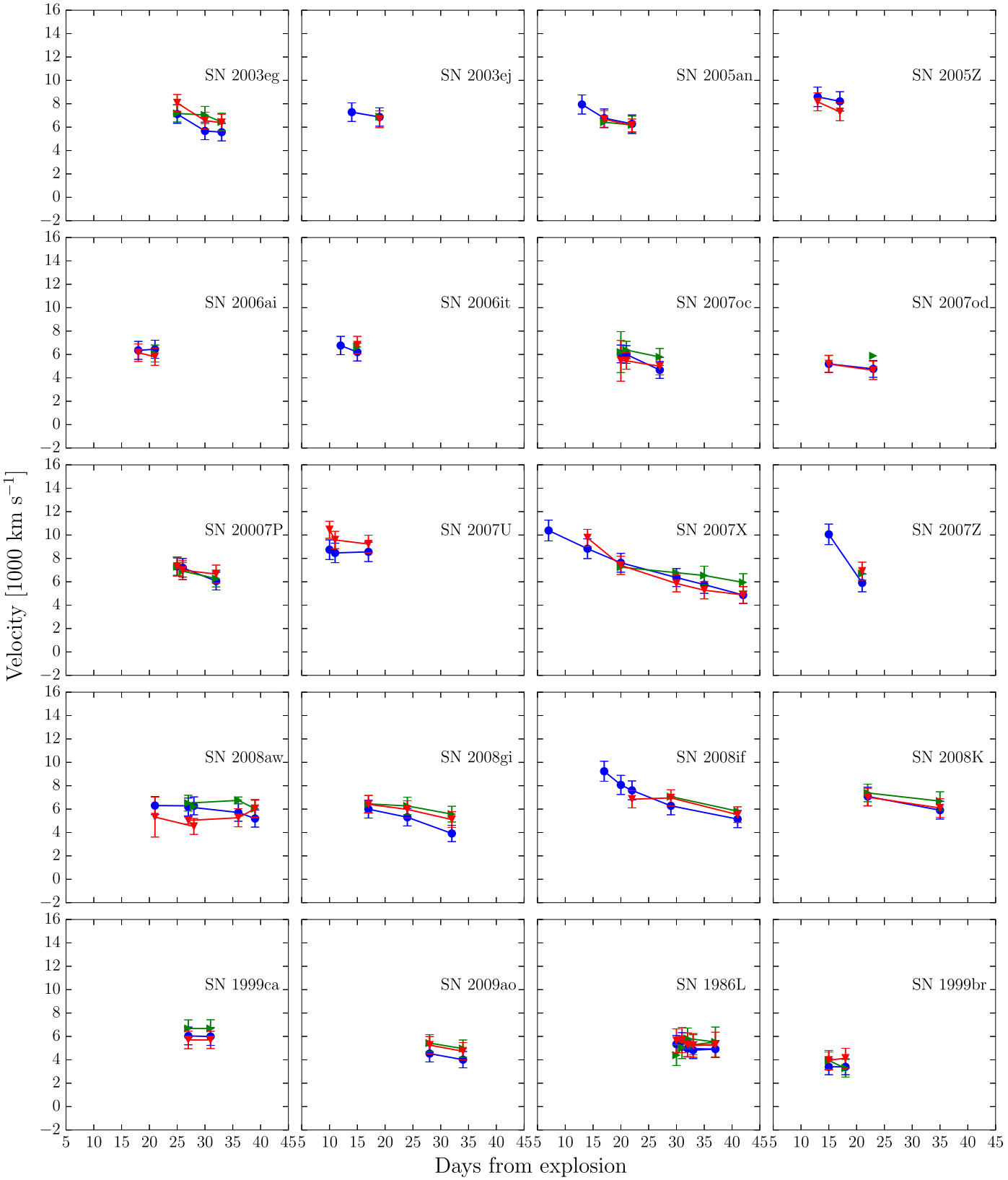

Figure 23. Velocity evolution of Cachito (blue) at early phases compared with Fe II λ5018 (green) and Fe II λ5169 (red).

and Na I D have the highest values (from 0 to ∼120), while Fe II λ4924, Fe II λ5018, Sc II/Fe II, the Sc II multiplet, Ba II, Sc II, and O I have the lowest ones (from 0 to ∼50).

The a/e evolution is displayed in Figure 22. One can see an increase until ∼60 days and then, the quantity remains constant or slightly decreases.

8.4. Cachito: Hydrogen HV Features or Si II Line

The nature of Cachito has recently been studied. Its presence on the blue side of H_α has given rise to multiple interpretations, such as HV features of hydrogen (e.g., Baron et al. 2000; Leonard et al. 2002b; Chugai et al. 2007; Inserra et al. 2011) or Si II λ6355 (e.g., Pastorello et al. 2006; Tomasella et al. 2013; Valenti et al. 2014). From our sample, 70 SNe show Cachito in the photospheric phase, between 7 and 120 days post-explosion; however, its behavior, shape, and evolution is different depending on the phase. To investigate the nature of Cachito, we examine the following possibilities.

1. If Cachito is produced by Si II, its velocity should be similar to those presented by other metal lines.
2. If Cachito is related to HV features of hydrogen, its velocity should be almost the same as those obtained from H_α at early phases. In addition, if it is present, a counterpart should be visible on the blue side of H_β.

Analyzing our sample, we can detect Cachito in 50 SNe at early phases (before 40 days). Because of the high temperatures at these epochs, the presence of Ba II λ6497 is discarded. Assuming that Cachito is produced by Si II, we find that 60% of SNe present a good match with Fe II λ5018 and Fe II λ5169 velocities.[30] Conversely, the rest of the sample shows velocities comparable to those measured at very early phases for H_α. Curiously, the Cachito shape is different between the two SN groups. In the former, the line is deeper and broader, while, in the latter, the line is shallow. In Figure 23, we present the velocity comparison for the former group, where a good agreement is found between Cachito, assumed as Si II λ6355 (blue), and the iron lines, Fe II λ5018 (green) and Fe II λ5169 (red).

Later than 40 days, we detect Cachito in 43 SNe. Proceeding with the velocity comparison, we can discard its identification as Si II or Ba II λ6497 (the latter, visible in few SNe from 60 days, see Figure 21), which suggests that Cachito is associated to hydrogen. During the plateau, it is possible to see Cachito as a shallow absorption feature only in H_α and/or as a narrow and deeper absorption on the blue side of both H_α and H_β (see an example in Figure 24). According to Chugai et al. (2007), the interaction between the SN ejecta and the RSG wind should result in the emergence of these HV absorption features. They argue that the existence of a shallow absorption feature is the result of the enhanced excitation of the outer unshocked ejecta, which is visible on the blue side of H_α (and He I λ10830). At early times, the H_β Cachito feature is not predicted by Chugai et al. (2007), who argue that the optical depth is too low at the line-forming region. They also discuss that in addition to the HV shallow absorption, an HV notch is formed in the cool dense shell (CDS) located behind the reverse shock. Given the relatively high H_α optical depth of the CDS, a counterpart could be seen in H_β as well. We found that 63% of the SNe with Cachito during the plateau show a counterpart in H_β with the same velocity as that presented on H_α, which favors the interpretation as CS interaction. The HV notch of H I is found in 27 SNe; however, in the low velocity/luminosity SNe, it is only present in H_α. After 50 days, the blue part of the spectrum (<5000 Å) is dominated by metal lines, which may hinder its detection. Nonetheless, we argue that these can be HV H I because at least one low velocity/luminosity SN, SN 2006ee, shows a Cachito feature on the blue side of both H_α and H_β, at around 50 days with consistent velocities. A summary of the analysis is displayed in Figure 25, where the H_α (red), HV H_α (blue), H_β (cyan), and HV H_β (green) velocity evolution is presented for 20 SNe.

In addition to the 70 SNe where Cachito can be identified either with Si II or HV features of H I, we find six SNe II that display Cachito at certain epochs; however, its exact properties do not align with the above interpretations (because of differences in shape and/or velocity). These are SN 2003bl, SN 2005an, SN 2007U, SN 2008br, SN 2002gd, and SN 2004fb. In summary, 59% of the full SNe sample show Cachito at some epoch, while 41% never show this feature. Soon after shock break-out, all SNe II have extremely high temperature ejecta. Therefore, if we were able to obtain spectral sequences shortly after explosion, the Si II feature would always be observed. However, observationally, this is not the case because there are many SNe II within our sample without Si II detections. This is simply an observational bias, due to the lack of data at very early times. Nevertheless, for SNe II that stay hotter for longer, the probability of detecting Si II becomes larger. We therefore speculate that SNe II that have detected Si II at early times have larger radii, which leads to a slower cooling of the ejecta and hence facilitates Si II detection. Interestingly, when we split the sample into those SNe II that do and do not display the Si II line, those where the line is detected are found to have lower a/e values, with only a 4% chance that the two populations are drawn from the same underlying distribution. This is also consistent with the previous finding that those SNe II with evident He I detections at around 20 days post-explosion are also found to have lower

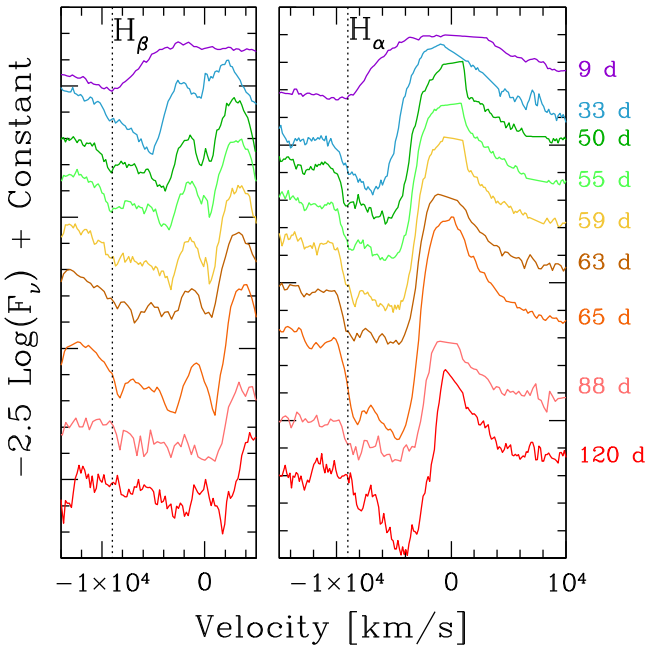

Figure 24. Spectral evolution of H_α and H_β lines of SN 2004fc. The dotted lines correspond to the HV features seen on the blue side of H_α and H_β from 50 to 120 days. We can see that the HV features show a velocity evolution from ~9000 to ~8000 km s^{-1}.

[30] Four SNe show a good match with Si II in very early phases, but between 30 and 40 days they do not show it. They also show a different shape.

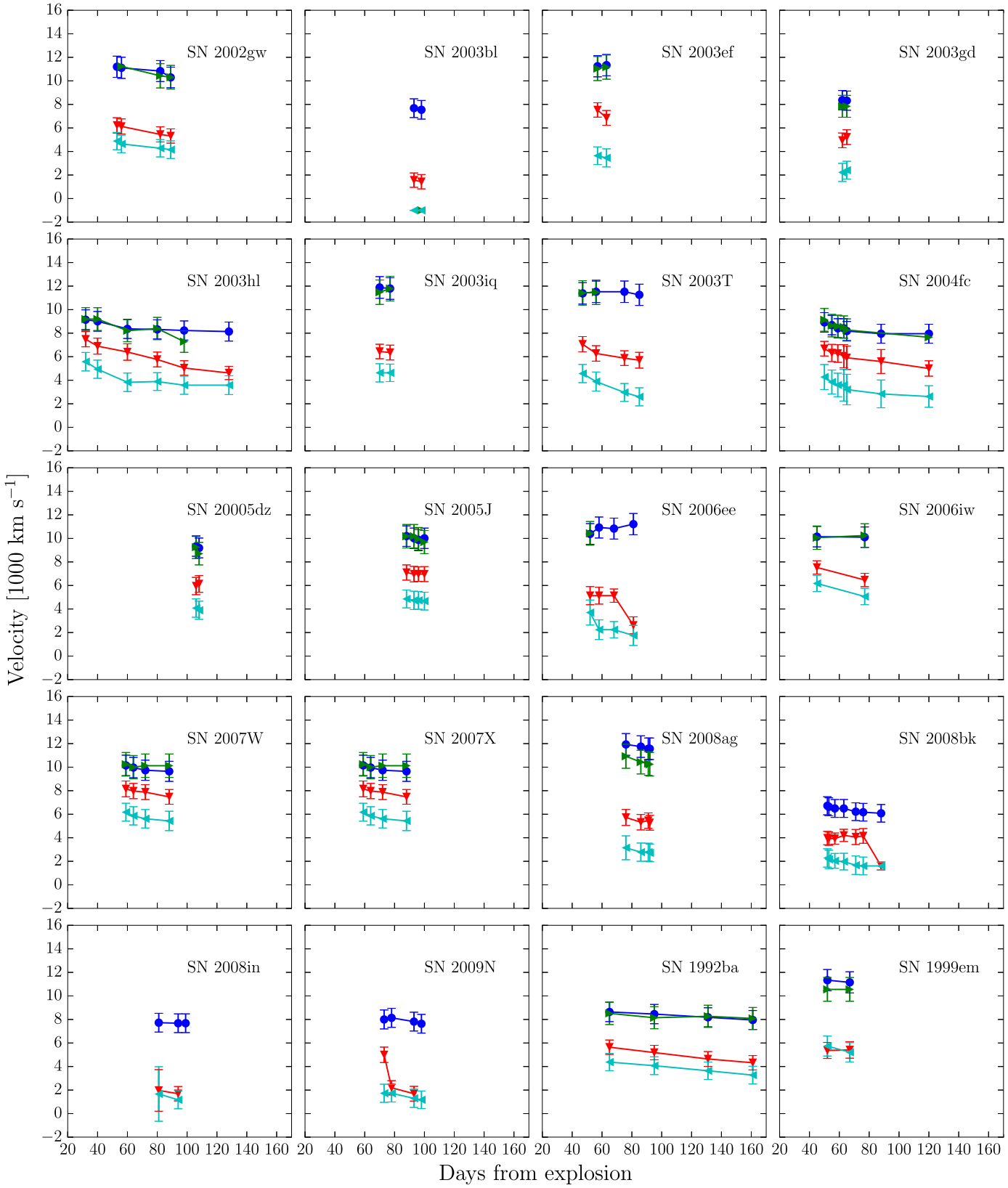

Figure 25. Velocity evolution of Cachito in the plateau phase compared with the Balmer lines. In blue: HV of H_α; in green: HV of H_β; in red: the H_α velocity; and in cyan: the H_β velocity.

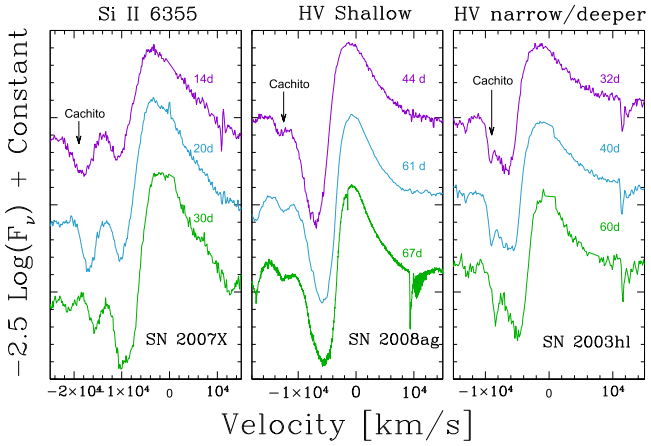

Figure 26. Cachito's shape according to its nature. Left panel: the Si II line in SN 2007X. Middle panel: HV features of H I as a shallow absorption in SN 2008ag. Right panel: HV features of H I as narrow and deeper absorption component in SN 2003hl.

a/e values, suggesting that the value of a/e is related to ejecta temperature evolution.

In the case of those SNe II displaying Cachito consistent with HV features, these are most likely produced by the interaction of the SN ejecta with the RSG wind, where the exact shape and persistence of Cachito is related to the wind density Chugai et al. (2007). In Figure 26, one can observe the significant diversity in the different detection of Cachito.

9. Conclusions

In this paper, we have presented optical spectra of 122 nearby SNe II observed between 1986 and 2009. A total of 888 spectra ranging between 3 and 363 days post-explosion have been analyzed. The spectral matching technique was discussed as an alternative to nondetection constraints for estimating SN explosion epochs.

In order to quantify the spectral diversity, we analyze the appearance of the photospheric lines and their time evolution in terms of the a/e and H_α velocity at the B-band transition time plus 10 days ($t_{\rm tran+10}$; see Gutiérrez et al. 2014 for more details), the magnitude at maximum ($M_{\rm max}$), the plateau decline (s_2), and metallicity (M13 N2). We analyzed the velocity decline rate of H_β, the a/e evolution, the expansion ejecta velocities, and the pEWs for 11 features: H_α, H_β, He I/Na I D, Fe II λ4924, Fe II λ5018, Fe II λ5169, Fe II blend, Sc II/Fe II, Sc II multiplet, Ba II, Sc II, and O I. We find a large range in velocities and pEWs, which may be related with a diversity in the explosion energy, radius of the progenitor, and metallicity. The evolution of line strengths was analyzed and compared to that of spectral models. SNe II displaying differences in spectral line evolution were also found to have other different spectral, photometric, and environmental properties. Finally, we discuss the detection and origin of Cachito on the blue side of H_α.

The main results obtained with our analysis are summarized as follows.

1. The line evolution indicates differences in temperatures and/or metallicity. Thus, SNe with slower temperature gradients show the appearance of the iron lines later, while SNe in environments with higher metallicities show them earlier. In fact, the Fe II line forest is present in faint SNe with low ejecta temperatures and/or in high metallicity environments. Comparing this result with the synthetic spectra, we find that indeed this feature is only present in higher metallicity (two times solar) and lower explosion energy models, which is consistent with our observations.
2. SNe II display a significant variety of expansion velocities, suggesting a large range in explosion energies.
3. At early phases (before 25 days), SNe II with a weak H_α absorption component show He I λ5876 and the Si II λ6355 features. We speculate that this occurs because of higher temperatures at these epochs.
4. Around 60% of our SNe II show the Cachito feature between 7 and 120 days since explosion. When Cachito is detected less than 30 days post-explosion, then it is identified with Si II. The epochs of early detection can thus inform us of the temperature evolution: SNe II with Si II detections at later epochs have higher temperatures, and this may be related to higher-radius progenitors. At later epochs, during the recombination phase, we suggest that Cachito is related to HV of hydrogen lines. Such HV features are most likely related to the interaction of the SN ejecta with the RSG wind.

All data analyzed in this work are available on http://csp.obs.carnegiescience.edu/, as well as the additional SNID templates (22 SNe), for the SNe II comparison.

C.P.G. and S.G.G. acknowledge support by projects IC120009 "Millennium Institute of Astrophysics (MAS)" and P10-064-F "Millennium Center for Supernova Science" of the Iniciativa Cientfica Milenio del Ministerio Economa, Fomento y Turismo de Chile. C.P.G. acknowledges support from EU/FP7-ERC grant No. [615929]. M.D.S. is supported by the Danish Agency for Science and Technology and Innovation realized through a Sapere Aude Level 2 grant and by a research grant (13261) from the VILLUM FONDEN. We gratefully acknowledge support of the CSP by the NSF under grants AST0306969, AST0908886, AST0607438, AST1008343, AST-1613472, AST-1613426, and AST-1613455. This research has made use of the NASA/IPAC Extragalactic Database (NED), which is operated by the Jet Propulsion Laboratory, California Institute of Technology, under contract with the National Aeronautics and Space Administration (NASA).

Appendix A
Additional Table

Appendix A presents additional information related to the observations and the analysis of our sample. Table 6 lists the spectroscopic observation information, Table 7 presents the explosion epoch estimation comparison, and Tables 8 and 9 present the mean velocity and mean pEW values, respectively.

Table 6
Spectroscopic Observation Information

UT Date	JD	Phase (days)	Tel.	Inst.	Wavelength Range (AA)	Resol. (AA)	Exp. (s)	Air-mass
(1)	(2)	(3)	(4)	(5)	(6)	(7)	(8)	(9)
				SN 1986L				
1986 Oct 09	2446712.50	4	⋯	⋯	3681–7728	⋯	1000	1.21
1986 Oct 11	2446714.50	6	⋯	⋯	3730–7168	⋯	1556	1.20
1986 Oct 12	2446715.50	7	⋯	⋯	3800–7322	⋯	2000	1.21
1986 Oct 13	2446716.50	8	⋯	⋯	3681–4988	⋯	1352	1.21[a]
1986 Oct 14	2446717.50	9	⋯	⋯	3681–4988	⋯	2500	1.19[a]
1986 Oct 15	2446718.50	10	⋯	⋯	3681–4988	⋯	2500	1.18[a]
1986 Oct 20	2446723.50	15	⋯	⋯	3720–5031	⋯	3000	1.24[a]
1986 Oct 26	2446729.50	21	⋯	⋯	3830–7330	⋯	2000	1.20
1986 Oct 28	2446731.50	23	⋯	⋯	3596–5125	⋯	2000	1.37
1986 Oct 28	2446731.50	23	⋯	⋯	3590–5130	⋯	⋯	1.37
1986 Oct 29	2446732.50	24	⋯	⋯	3675–5240	⋯	1200	1.23
1986 Nov 01	2446735.50	27	⋯	⋯	3270–7205	⋯	1800	1.21
1986 Nov 02	2446736.50	28	⋯	⋯	3270–7205	⋯	1200	1.2
1986 Nov 03	2446737.50	29	⋯	⋯	3847–7357	⋯	2000	1.22
1986 Nov 03	2446737.50	29	⋯	⋯	3270–7205	⋯	1200	1.21
1986 Nov 04	2446738.50	30	⋯	⋯	4166–7701	⋯	1800	1.22
1986 Nov 04	2446738.50	30	⋯	⋯	3270–7205	⋯	1200	1.20
1986 Nov 05	2446739.50	31	⋯	⋯	3270–7205	⋯	1200	1.20
1986 Nov 06	2446740.50	32	⋯	⋯	3270–7205	⋯	1200	1.21
1986 Nov 07	2446741.50	33	⋯	⋯	3270–7205	⋯	1200	1.21
1986 Nov 10	2446744.50	36	⋯	⋯	4166–7701	⋯	1800	1.23
1986 Nov 11	2446745.50	37	⋯	⋯	3830–7285	⋯	1000	1.19
1986 Nov 14	2446748.50	40	⋯	⋯	3561–6446	⋯	⋯	1.20
1986 Nov 16	2446750.50	42	⋯	⋯	3561–6446	⋯	⋯	1.18
1986 Nov 25	2446759.50	51	⋯	⋯	3450–6950	⋯	2000	1.20[a]
1986 Dec 09	2446773.50	65	⋯	⋯	3680–6670	⋯	1000	1.44
1986 Dec 10	2446774.50	66	⋯	⋯	3769–7329	⋯	2262	⋯
1986 Dec 23	2446787.50	79	⋯	⋯	3991–7548	⋯	2394	⋯
1987 Jan 01	2446796.50	88	⋯	⋯	3776–7578	⋯	2545	⋯
1987 Jan 23	2446818.50	110	⋯	⋯	3450–6950	⋯	3000	1.20
1987 Jan 30	2446825.50	117	⋯	⋯	5601–7998	⋯	⋯	1.24

Notes.
Note that up to 1999, we do not have access to the telescope, intrument, and resolution information. Between 2002 and 2003, the resolution information is not available.
Columns: (1) UT date of the observation; (2) Julian date of the observation; (3) phase in days since explosion; (4) telescope code 3P6: ESO 3.6 m Telescope; BAA: Las Campanas *Magellan* I 6.5 m Baade Telescope; CLA: Las Campanas *Magellan* II 6.5 m Clay Telescope; DUP: Las Campanas 2.5 m du Pont Telescope Telescope; NTT: New Technology Telescope; (5) instrument code BC: Boller & Chivens spectrograph; EF: ESO Faint Object Spectrograph and Camera (EFOSC-2); EM: ESO Multi-Mode Instrument (EMMI); IM: Inamori *Magellan* Areal Camera and Spectrograph (IMACS), LD: Low Dispersion Survey Spectrograph (LDSS); WF: Wide Field Reimaging CCD Camera (WFCCD); (6) wavelength range covered; (7) spectral resolution in Å as estimated from arc-lamp lines; (8) total exposure time; (9) airmass at the middle of the observation.
[a] Spectra with low S/N.
[b] Spectra with defects resulting from the observing procedure or data reduction.

(This table is available in its entirety in machine-readable form.)

Table 7
Explosion Epoch Estimation Comparison

SN	Spect. Date JD	Best Match	Days from Maximum	Days from Explosion	Average (Using Match)	Explosion Date (MJD)	Nondetection Date (MJD)	Discovery Date (MJD)	Explosion Date (MJD)	Difference (days)
1968L	46715.5	2006bp	−2	7	7	46708.5 (5)	46705.5	46710.5	46708.0 (3)	0
		1999em	−4	6						
1988A	47188.5	1999em	+5	15	17	47171.5 (6)	47175.5	47179.0	47177.2 (2)	−6
		2006bp	+7	16						
		2004et	+4	20						
1990E	47945.5	1999em	−3	7	9	47936.5 (6)	47932.5	47937.7	47935.1 (3)	1
		2004et	−3	13						
		1999gi	−4	8						
		2006bp	0	9						
1990K	48049.5	2004et	+33	49	48	48001.5 (6)	⋯	48037.3	⋯	⋯
		2006bp	+49	58						
		1999em	+27	37						
1991al	48473.5	2006bp	+25	34	31	48442.5 (8)	⋯	48453.7	⋯	⋯
		2004et	+20	36						
		1999em	+16	26						
		2003iq	⋯	29						
1992af	48832.8	2003bn	⋯	35	34	48798.8 (8)	⋯	48802.8	⋯	⋯
		2007il	⋯	45						
		1999gi	+19	31						
		2006bp	+20	29						
		2003iq	⋯	29						
		2004et	+20	36						

Note.
Columns: (1) SN name; (2) reduced Julian date of the spectrum used to the match (JD 2,400,000); (3) best match obtained with SNID; (4) days from maximum of the template used to the match; (5) days from explosion of the template used to the match; (6) average obtained from the days from explosion; (7) explosion date obtained with the matching technique; (8) nondetection date of the SN; (9) discovery date of the SN; (10) explosion date obtained from nondetection and discovery date; (11) difference in days between the explosion date from matching technique and nondetection.

(This table is available in its entirety in machine-readable form.)

Table 8
Mean Velocity Values and the Standard Deviation for Our Sample

Epoch (Days)	H_α (km s^{-1})	H_α (km s^{-1})	H_β (km s^{-1})	Fe II λ4924 (km s^{-1})	Fe II λ5018 (km s^{-1})	Fe II λ5169 (km s^{-1})	Fe II/Sc II (km s^{-1})	Sc II Mult. (km s^{-1})	Na I D (km s^{-1})	Ba II (km s^{-1})	Sc II (km s^{-1})	O I (km s^{-1})
4	8369 ± 3930	12845 ± 950	11379 ± 1800	...	...	...	...	...	...	...	...	...
8.6	9399 ± 3564	10702 ± 1382	9605 ± 1574	...	...	10447 ± 1050	...	...	...	...	...	...
12.8	9384 ± 2240	9468 ± 1787	8748 ± 1653	3187 ± 281	5298 ± 1791	6871 ± 2234	...	...	...	...	...	3280 ± 1680
18.1	9044 ± 1576	8987 ± 1430	8364 ± 1478	3183 ± 796	6237 ± 1117	6300 ± 1174	...	...	...	...	...	4888 ± 2762
23.1	7191 ± 2027	7798 ± 1966	7083 ± 1690	3882 ± 1025	5241 ± 1328	5274 ± 1254	5057 ± 1995	5426 ± 1612	...	5539 ± 3200	5076 ± 420	3951 ± 1396
27.7	7728 ± 1606	8369 ± 1825	7426 ± 1527	4193 ± 1499	5506 ± 1229	5440 ± 1098	6033 ± 2276	5747 ± 1826	...	4984 ± 2790	4537 ± 2678	4961 ± 1900
33.1	7319 ± 1190	7745 ± 1194	6668 ± 1260	4240 ± 1139	4974 ± 1114	4942 ± 892	5085 ± 1307	4832 ± 1267	5865 ± 2029	4521 ± 1595	4504 ± 1323	4908 ± 1586
38.1	6815 ± 1563	7478 ± 1548	6297 ± 1582	4135 ± 1346	4641 ± 1324	4428 ± 1065	4835 ± 1458	4427 ± 1181	5479 ± 1977	3979 ± 1513	3837 ± 1301	4274 ± 1737
42.8	6188 ± 1807	6551 ± 1745	5267 ± 1600	3544 ± 1158	3857 ± 1097	3760 ± 1045	3969 ± 1188	3739 ± 968	4411 ± 1596	3164 ± 1367	3621 ± 1238	3587 ± 1605
47.8	6616 ± 1864	7145 ± 1772	5541 ± 1688	3493 ± 1130	4049 ± 1181	3938 ± 990	4243 ± 1035	3956 ± 899	4952 ± 1634	3712 ± 1165	3747 ± 888	4090 ± 947
53.1	5975 ± 1457	6535 ± 1755	5004 ± 1785	3307 ± 1027	3654 ± 1135	3537 ± 851	3888 ± 1181	3507 ± 978	4408 ± 1531	3258 ± 1258	3227 ± 1146	3520 ± 1690
58.6	5907 ± 1883	6615 ± 1900	5025 ± 1774	3086 ± 924	3682 ± 1358	3631 ± 973	3803 ± 1371	3552 ± 935	4491 ± 1467	3047 ± 815	3092 ± 638	2861 ± 1099
63.3	5836 ± 1597	6619 ± 1565	4836 ± 1548	3074 ± 919	3455 ± 1093	3401 ± 758	3553 ± 1073	3294 ± 918	4284 ± 1213	3062 ± 735	3145 ± 898	2919 ± 1077
68	5556 ± 1053	6613 ± 1038	4909 ± 1146	2963 ± 464	3378 ± 722	3397 ± 639	3342 ± 609	3099 ± 752	4359 ± 1098	2785 ± 581	2843 ± 593	2786 ± 1095
72.8	5473 ± 1496	6720 ± 1564	4725 ± 1665	2875 ± 936	3203 ± 952	3374 ± 828	3352 ± 1315	3074 ± 935	4296 ± 1426	3004 ± 1123	2738 ± 813	3091 ± 1631
78.2	5037 ± 1706	6061 ± 1660	4460 ± 1553	2685 ± 784	2980 ± 778	3078 ± 820	2981 ± 852	2841 ± 850	4229 ± 1344	2792 ± 877	2607 ± 668	2682 ± 1109
83.5	5687 ± 1722	6490 ± 1883	4386 ± 1492	2679 ± 929	2863 ± 1000	3074 ± 919	2686 ± 861	2734 ± 700	4240 ± 1156	2564 ± 776	2428 ± 773	2232 ± 424
87.5	4871 ± 1664	6197 ± 1930	4448 ± 1514	2732 ± 807	3217 ± 937	3253 ± 785	3041 ± 855	2679 ± 532	4335 ± 1062	2735 ± 724	2517 ± 722	2986 ± 16344
93.3	4627 ± 1541	5666 ± 2016	4261 ± 1493	2555 ± 372	2841 ± 811	2946 ± 718	2607 ± 610	2478 ± 596	4200 ± 1059	2484 ± 554	2256 ± 398	2493 ± 12364
98.2	4349 ± 1602	5788 ± 2073	4372 ± 1505	2122 ± 550	2498 ± 603	2476 ± 631	2276 ± 644	2069 ± 629	4203 ± 971	2139 ± 501	1929 ± 580	1655 ± 950
103	3466 ± 836	4422 ± 1353	3014 ± 993	2067 ± 593	2141 ± 393	2119 ± 525	1844 ± 471	1864 ± 334	3445 ± 915	101 ± 506	1514 ± 124	1335 ± 321
108.2	4114 ± 836	5625 ± 1226	4128 ± 885	2128 ± 594	2430 ± 346	2625 ± 457	2531 ± 344	2278 ± 242	4073 ± 388	274 ± 259	2161 ± 249	1833 ± 1555
115.7	4927 ± 1763	5805 ± 1176	4536 ± 1025	2667 ± 484	2623 ± 725	2451 ± 679	2170 ± 1860	1748 ± 210	4793 ± 722	100 ± 108	1441 ± 220	1823 ± 1160

Note. Columns: (1) epoch; (2) velocity of H_α from FWHM of emission component; (3) velocity of H_α from the minimum flux of the absorption component; (4) velocity of H_β; (5) velocity of Fe II λ4924; (6) velocity of Fe II λ5018; (7) velocity of Fe II λ5169; (8) velocity of Fe II/Sc II; (9) velocity of Sc II Multiplet; (10) velocity of Na I D; (11) velocity of Ba II; (12) velocity of ScII; and (13) velocity of O I.

Table 9
Mean pEW Values and the Stardard Deviations for Our Sample

Epoch (Days)	H_α (Å)	$H_{5\alpha}$ (Å)	H_β (Å)	Fe II λ4924 (Å)	Fe II λ5018 (Å)	Fe II λ5169 (Å)	Fe II/Sc II (Å)	Sc II Mult. (Å)	Na I D (Å)	Ba II (Å)	Sc II (Å)	O I (Å)
4	0.8 ± 1.8	47.3 ± 28.7	11.9 ± 8.3	0 ± 0	0 ± 0	0 ± 0	0 ± 0	0 ± 0	···	0 ± 0	0 ± 0	···
8.6	4.34 ± 5.4	83.2 ± 46.4	24.8 ± 19.2	0 ± 0	0 ± 0	0.1 ± 0.6	0 ± 0	0 ± 0	···	0 ± 0	0 ± 0	···
12.8	8.6 ± 10.9	121.2 ± 61.2	33.3 ± 17.6	0.3 ± 1.3	1.2 ± 3.2	5.5 ± 8.6	0 ± 0	0 ± 0	···	0 ± 0	0 ± 0	11 ± 1.1
18.1	16.6 ± 17.3	157.2 ± 53.7	37.4 ± 14.8	0.2 ± 0.8	4.2 ± 4.8	14.5 ± 14.0	0 ± 0	0 ± 0	···	0 ± 0	0 ± 0	5.67 ± 1.1
23.1	25.7 ± 22.1	147.8 ± 62.2	43.3 ± 18.8	1.4 ± 2.5	9.3 ± 5.5	22.4 ± 10.9	1.1 ± 2.5	1.02 ± 3.21	···	0.1 ± 0.3	0.1 ± 0.30	11.5 ± 8.6
27.7	25.0 ± 25.9	142.7 ± 55.2	43.8 ± 16.7	1.1 ± 2.5	9.6 ± 4.5	25.5 ± 9.5	1.4 ± 3.1	1.61 ± 3.99	···	0.3 ± 1.0	0.5 ± 1.40	10.9 ± 5.6
33.1	36.6 ± 20.4	155.7 ± 44.5	49.2 ± 13.6	2.8 ± 3.6	12.5 ± 4.0	30.2 ± 8.4	4.9 ± 4.4	6.48 ± 6.30	13.3 ± 7.6	1.1 ± 2.7	2.1 ± 3.17	9.8 ± 5.8
38.1	42.5 ± 23.3	152.9 ± 44.2	50.2 ± 16.4	3.8 ± 3.8	14.5 ± 6.0	33 ± 13.5	6.0 ± 5.0	8.09 ± 7.14	15.6 ± 8.3	2.0 ± 3.4	2.8 ± 4.00	10.6 ± 3.9
42.8	46.1 ± 22.7	142.0 ± 64.0	49.2 ± 15.9	6.1 ± 4.2	15.1 ± 5.4	32.9 ± 9.2	7.1 ± 4.8	10.5 ± 5.87	18.7 ± 10.3	2.8 ± 3.9	3.7 ± 3.77	11.0 ± 5.5
47.8	48.1 ± 21.6	169 ± 61.7	54.2 ± 18.3	6.4 ± 4.1	14.2 ± 5.8	34.6 ± 9.6	7.9 ± 3.3	11.5 ± 4.83	26.5 ± 12.5	4.3 ± 4.7	5.1 ± 3.26	13.0 ± 4.9
53.1	56.6 ± 21.7	156.9 ± 55.2	48.8 ± 20.3	8.1 ± 5.5	17.9 ± 5.9	40.2 ± 13.5	10.1 ± 4.7	14.0 ± 7.53	32.4 ± 15.2	5.6 ± 4.7	7.2 ± 5.64	11.9 ± 5.9
58.5	50.7 ± 24.9	169.7 ± 78.6	49.6 ± 26.4	7.5 ± 4.7	18.3 ± 7.4	39.8 ± 15.7	11.2 ± 5.5	16.0 ± 8.35	38.3 ± 20.0	6.4 ± 6.2	6.7 ± 5.09	11.1 ± 5.8
63.3	58.1 ± 18.4	173.3 ± 70.1	49.5 ± 25.1	9.7 ± 5.7	19.8 ± 5.6	44.1 ± 11.0	11.8 ± 5.3	18.2 ± 7.63	46.0 ± 17.5	7.9 ± 6.8	7.4 ± 4.78	10.8 ± 4.6
68.0	60.2 ± 17.3	163.3 ± 42.1	53.1 ± 27.0	9.4 ± 6.0	21.6 ± 7.0	42.8 ± 9.6	13.6 ± 6.1	19.5 ± 7.79	52.2 ± 17.1	8.2 ± 6.3	8.0 ± 5.88	12.1 ± 4.5
72.8	65.2 ± 20.8	179.5 ± 71.8	56.3 ± 32.2	9.6 ± 6.3	19.5 ± 6.3	41 ± 11.7	11.5 ± 5.9	17.3 ± 8.15	49.4 ± 24.5	8.1 ± 6.9	6.9 ± 5.61	14.3 ± 7.1
78.2	60.0 ± 21.4	167.0 ± 71.7	46.9 ± 26.1	11.6 ± 6.6	20.8 ± 7.8	42.4 ± 10.1	14.7 ± 5.2	22.9 ± 7.55	59.7 ± 21.8	12.6 ± 7.56	11.4 ± 4.7	12.7 ± 5.6
83.5	53.8 ± 31.1	202.2 ± 86.1	52.4 ± 27.9	10.4 ± 5.9	21.5 ± 7.8	47.0 ± 13.5	14.3 ± 5.2	21.3 ± 8.00	63.9 ± 28.6	12.8 ± 9.41	11.4 ± 7.4	11.1 ± 3.7
87.5	56.1 ± 26.9	176.4 ± 95.0	55.2 ± 28.8	10.5 ± 7.6	23.0 ± 7.5	51.3 ± 12.8	14.9 ± 6.2	21.6 ± 9.26	63.2 ± 19.0	11.4 ± 7.67	10.1 ± 6.5	15.4 ± 6.9
93.3	50.9 ± 28.8	182.9 ± 107.3	47.0 ± 26.7	13.3 ± 8.1	25.6 ± 8.2	48.2 ± 11.1	17.3 ± 7.7	27.3 ± 10.6	69.7 ± 17.7	16.6 ± 12.4	12.4 ± 6.5	11.5 ± 5.8
98.2	61.6 ± 28.3	214.4 ± 117.6	62.7 ± 29.3	14.9 ± 4.7	26.2 ± 7.0	46.4 ± 9.9	17.7 ± 6.2	27.6 ± 7.81	81.8 ± 26.4	17.6 ± 10.2	12.9 ± 6.7	12.4 ± 2.7
103.0	48.2 ± 25.9	184.8 ± 80.3	41.2 ± 24.8	19.1 ± 4.7	30.7 ± 3.9	48.8 ± 6.4	16.8 ± 6.6	26.4 ± 9.00	76.0 ± 14.9	34.6 ± 9.78	16.5 ± 4.0	11.8 ± 1.6
108.2	60.1 ± 19.0	208.9 ± 56.1	43.8 ± 15.5	15.9 ± 4.0	25.7 ± 2.6	41 ± 10.2	15.0 ± 0.0	21.5 ± 4.11	69.2 ± 20.8	20.3 ± 15.7	9.8 ± 2.7	13.0 ± 2.8
115.7	46.2 ± 18.6	287.5 ± 158.8	53.4 ± 29.4	7.9 ± 0.9	16.8 ± 6.2	35.1 ± 12.9	21.2 ± 3.5	16.3 ± 4.5	70.2 ± 23.1	22.4 ± 15.7	6.7 ± 4.5	8.9 ± 1.5

Note. Columns: (1) SN name; (2) pEW of H_α absorption component; (3) pEW of H_α emission component; (4) pEW of H_β; (5) pEW of Fe II λ4924; (6) pEW of Fe II λ5018; (7) pEW of Fe II λ5169; (8) pEW of Fe II/Sc II; (9) pEW of Sc II Multiplet; (10) pEW of Na I D; (11) pEW of Ba II; (12) pEW of ScII; (13) pEW of O I.

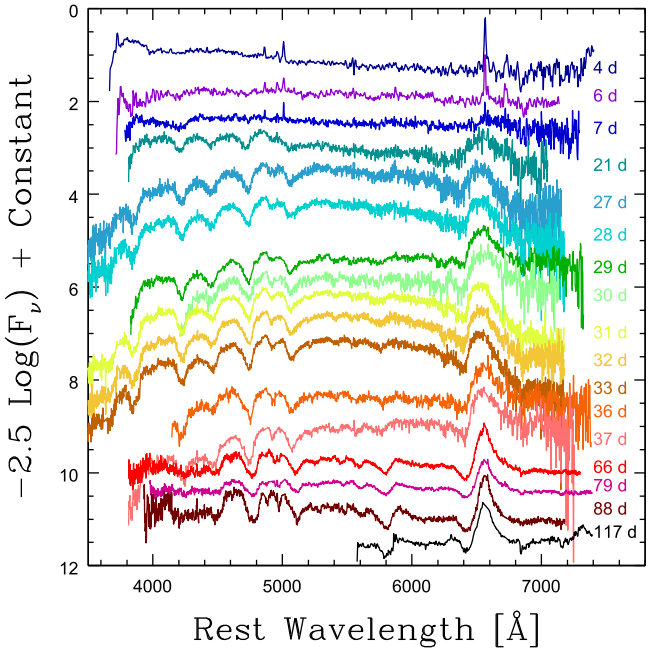

Figure 27. SNe II SN 1986L spectra.

(The complete figure set (120 images) is available.)

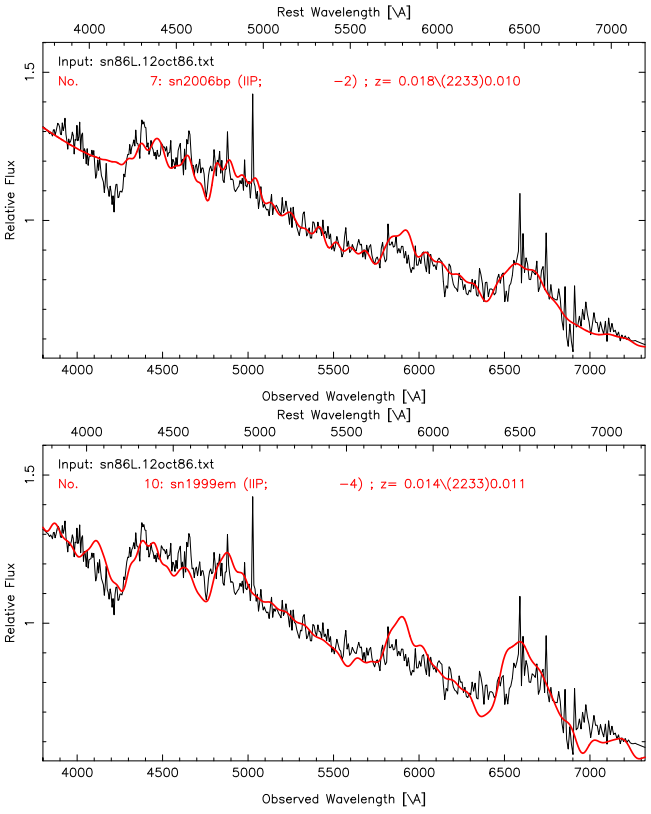

Figure 28. Best spectral matching of SN 1986L using SNID. The plots show SN 1986L compared with SN 2006bp and SN 1999em at 6 and 7 days from explosion.

(The complete figure set (430 images) is available.)

Appendix B
Spectral Series

In this section, the spectral time-series for all SNe in our sample are presented. Figure 27 shows an example of the spectral evolution of SN 1986L. Plots for the full sample can be found in the online version.

Appendix C
SNID Matches

In this section, we present the best spectral matching plots for each SN in our sample. An example of this technique is shown in Figure 28 for SN 1986L. Plots for the full sample can be found in the online version.

ORCID iDs

Claudia P. Gutiérrez https://orcid.org/0000-0002-7252-4351
Joseph P. Anderson https://orcid.org/0000-0003-0227-3451
Nidia Morrell https://orcid.org/0000-0003-2535-3091
Maximilian D. Stritzinger https://orcid.org/0000-0002-5571-1833
Mark M. Phillips https://orcid.org/0000-0003-2734-0796
Lluis Galbany https://orcid.org/0000-0002-1296-6887
Luc Dessart https://orcid.org/0000-0003-0599-8407
Massimo Della Valle https://orcid.org/0000-0003-3142-5020
Eric Y. Hsiao https://orcid.org/0000-0003-1039-2928
Kevin Krisciunas https://orcid.org/0000-0002-6650-694X
Barry F. Madore https://orcid.org/0000-0002-1576-1676
Jose Luis Prieto https://orcid.org/0000-0003-0943-0026
Enrico Cappellaro https://orcid.org/0000-0001-5008-8619
Alessandro Pizzella https://orcid.org/0000-0001-9585-417X

References

Allington-Smith, J., Breare, M., Ellis, R., et al. 1994, PASP, 106, 983
Anderson, J. P., Dessart, L., Gutierrez, C. P., et al. 2014a, MNRAS, 441, 671
Anderson, J. P., Gutiérrez, C. P., Dessart, L., et al. 2016, A&A, 589, A110
Anderson, J. P., González-Gaitán, S., Hamuy, M., et al. 2014b, ApJ, 786, 67
Arcavi, I., Gal-Yam, A., Kasliwal, M. M., et al. 2010, ApJ, 721, 777
Barbon, R., Buondí, V., Cappellaro, E., & Turatto, M. 1999, A&AS, 139, 531
Barbon, R., Ciatti, F., & Rosino, L. 1979, A&A, 72, 287
Baron, E., Branch, D., Hauschildt, P. H., et al. 2000, ApJ, 545, 444
Blanco, V. M., Gregory, B., Hamuy, M., et al. 1987, ApJ, 320, 589
Blondin, S., & Tonry, J. L. 2007, ApJ, 666, 1024
Bose, S., Kumar, B., Sutaria, F., et al. 2013, MNRAS, 433, 1871
Branch, D., Falk, S. W., Uomoto, A. K., et al. 1981, ApJ, 244, 780
Buta, R. J. 1982, PASP, 94, 578
Buzzoni, B., Delabre, B., Dekker, H., et al. 1984, Msngr, 38, 9
Cappellaro, E., Danziger, I. J., della Valle, M., Gouiffes, C., & Turatto, M. 1995, A&A, 293, 723
Chugai, N. N., Chevalier, R. A., & Utrobin, V. P. 2007, ApJ, 662, 1136
Contreras, C., Hamuy, M., Phillips, M. M., et al. 2010, AJ, 139, 519
Dall'Ora, M., Botticella, M. T., Pumo, M. L., et al. 2014, ApJ, 787, 139
Dekker, H., Delabre, B., & Dodorico, S. 1986, Proc. SPIE, 627, 339
Dessart, L., Blondin, S., Brown, P. J., et al. 2008, ApJ, 675, 644
Dessart, L., & Hillier, D. J. 2005, A&A, 437, 667
Dessart, L., & Hillier, D. J. 2006, A&A, 447, 691
Dessart, L., & Hillier, D. J. 2008, MNRAS, 383, 57
Dessart, L., & Hillier, D. J. 2010, MNRAS, 405, 2141
Dessart, L., & Hillier, D. J. 2011, MNRAS, 410, 1739
Dessart, L., Hillier, D. J., Waldman, R., & Livne, E. 2013, MNRAS, 433, 1745
Dressler, A., Bigelow, B., Hare, T., et al. 2011, PASP, 123, 288

Dwek, E. 1983, ApJ, 274, 175
Fabbri, J., Otsuka, M., Barlow, M. J., et al. 2011, MNRAS, 418, 1285
Faran, T., Poznanski, D., Filippenko, A. V., et al. 2014a, MNRAS, 445, 554
Faran, T., Poznanski, D., Filippenko, A. V., et al. 2014b, MNRAS, 442, 844
Fesen, R. A., Gerardy, C. L., Filippenko, A. V., et al. 1999, AJ, 117, 725
Filippenko, A. V., Matheson, T., & Ho, L. C. 1993, ApJL, 415, L103
Folatelli, G., Morrell, N., Phillips, M. M., et al. 2013, ApJ, 773, 53
Folatelli, G., Phillips, M. M., Burns, C. R., et al. 2010, AJ, 139, 120
Fransson, C., & Chevalier, R. A. 1987, ApJL, 322, L15
Galbany, L., Hamuy, M., Phillips, M. M., et al. 2016, AJ, 151, 33
Gutiérrez, C. P., Anderson, J. P., Hamuy, M., et al. 2014, ApJL, 786, L15
Hamuy, M. 2003, ApJ, 582, 905
Hamuy, M., Folatelli, G., Morrell, N. I., et al. 2006, PASP, 118, 2
Hamuy, M., Maza, J., Phillips, M. M., et al. 1993, AJ, 106, 2392
Hamuy, M., Phillips, M. M., Suntzeff, N. B., et al. 1996, AJ, 112, 2438
Hamuy, M., & Pinto, P. A. 2002, ApJL, 566, L63
Hamuy, M., Pinto, P. A., Maza, J., et al. 2001, ApJ, 558, 615
Hamuy, M., Suntzeff, N. B., Gonzalez, R., & Martin, G. 1988, AJ, 95, 63
Hamuy, M. A. 2001, PhD thesis, Univ. Arizona
Harutyunyan, A. H., Pfahler, P., Pastorello, A., et al. 2008, A&A, 488, 383
Howell, D. A., Sullivan, M., Perrett, K., et al. 2005, ApJ, 634, 1190
Immler, S., Fesen, R. A., Van Dyk, S. D., et al. 2005, ApJ, 632, 283
Inserra, C., Pastorello, A., Turatto, M., et al. 2013, A&A, 555, A142
Inserra, C., Turatto, M., Pastorello, A., et al. 2011, MNRAS, 417, 261
Inserra, C., Turatto, M., Pastorello, A., et al. 2012, MNRAS, 422, 1122
Jerkstrand, A., Fransson, C., Maguire, K., et al. 2012, A&A, 546, A28
Jerkstrand, A., Smartt, S. J., Fraser, M., et al. 2014, MNRAS, 439, 3694
Jones, M. I., Hamuy, M., Lira, P., et al. 2009, ApJ, 696, 1176
Kotak, R., Meikle, W. P. S., Farrah, D., et al. 2009, ApJ, 704, 306
Leonard, D. C., Filippenko, A. V., Gates, E. L., et al. 2002b, PASP, 114, 35
Leonard, D. C., Filippenko, A. V., Li, W., et al. 2002a, AJ, 124, 2490
Li, W., Van Dyk, S. D., Filippenko, A. V., & Cuillandre, J.-C. 2005, PASP, 117, 121
Lisakov, S. M., Dessart, L., Hillier, D. J., Waldman, R., & Livne, E. 2017, MNRAS, 466, 34
Maguire, K., Di Carlo, E., Smartt, S. J., et al. 2010, MNRAS, 404, 981
Marino, R. A., Rosales-Ortega, F. F., Sánchez, S. F., et al. 2013, A&A, 559, A114
Maund, J. R., & Smartt, S. J. 2005, MNRAS, 360, 288
Menzies, J. W., Catchpole, R. M., van Vuuren, G., et al. 1987, MNRAS, 227, 39P
Minkowski, R. 1941, PASP, 53, 224
Misra, K., Pooley, D., Chandra, P., et al. 2007, MNRAS, 381, 280
Müller, T., Prieto, J. L., Pejcha, O., & Clocchiatti, A. 2017, ApJ, 841, 127
Olivares, F. 2008, MSc thesis, Univ. Chile (arXiv:0810.5518)
Pastorello, A., Sauer, D., Taubenberger, S., et al. 2006, MNRAS, 370 1752
Pastorello, A., Valenti, S., Zampieri, L., et al. 2009, MNRAS, 394, 2266
Pastorello, A., Zampieri, L., Turatto, M., et al. 2004, MNRAS, 347, 74
Patat, F., Barbon, R., Cappellaro, E., & Turatto, M. 1994, A&A, 282, 731
Pejcha, O., & Prieto, J. L. 2015a, ApJ, 799, 215
Pejcha, O., & Prieto, J. L. 2015b, ApJ, 806, 225
Phillips, M. M., Heathcote, S. R., Hamuy, M., & Navarrete, M. 1988, AJ, 95, 1087
Pooley, D., Lewin, W. H. G., Fox, D. W., et al. 2002, ApJ, 572, 932
Roy, R., Kumar, B., Benetti, S., et al. 2011, ApJ, 736, 76
Sahu, D. K., Anupama, G. C., Srividya, S., & Muneer, S. 2006, MNRAS, 372, 1315
Sanders, N. E., Soderberg, A. M., Gezari, S., et al. 2015, ApJ, 799, 208
Schlafly, E. F., & Finkbeiner, D. P. 2011, ApJ, 737, 103
Schlegel, E. M. 1990, MNRAS, 244, 269
Schmidt, B. P., Kirshner, R. P., Schild, R., et al. 1993, AJ, 105, 2236
Smartt, S. J. 2015, PASA, 32, e016
Smartt, S. J., Eldridge, J. J., Crockett, R. M., & Maund, J. R. 2009, MNRAS, 395, 1409
Smartt, S. J., Maund, J. R., Hendry, M. A., et al. 2004, Sci, 303, 499
Spiro, S., Pastorello, A., Pumo, M. L., et al. 2014, MNRAS, 439, 2873
Stritzinger, M. D., Anderson, J. P., Contreras, C., et al. 2017, arXiv:1707.07616
Stritzinger, M. D., Phillips, M. M., Boldt, L. N., et al. 2011, AJ, 142, 156
Suntzeff, N. B., Hamuy, M., Martin, G., Gomez, A., & Gonzalez, R. 1988, AJ, 96, 1864
Taddia, F., Stritzinger, M. D., Bersten, M., et al. 2017, A&A, submitted (arXiv:1707.07614)
Taddia, F., Stritzinger, M. D., Sollerman, J., et al. 2012, A&A, 537 A140
Taddia, F., Stritzinger, M. D., Sollerman, J., et al. 2013, A&A, 555, A10
Tomasella, L., Cappellaro, E., Fraser, M., et al. 2013, MNRAS, 434, 1636
Turatto, M., Cappellaro, E., Benetti, S., & Danziger, I. J. 1993, MNRAS, 265, 471
Valenti, S., Howell, D. A., Stritzinger, M. D., et al. 2016, MNRAS, 459 3939
Valenti, S., Sand, D., Pastorello, A., et al. 2014, MNRAS, 438, L101
Van Dyk, S. D., Li, W., & Filippenko, A. V. 2003, PASP, 115, 1289
Wood-Vasey, W. M., Aldering, G., Lee, B. C., et al. 2004, NewAR, 48, 637